Received: 5 May 2023 | Revised: 18 August 2023 | Accepted: 22 October 2023

DOI: 10.1002/rob.22265

RESEARCH ARTICLE

WILEY

Design and field test of a foldable wing unmanned aerial–underwater vehicle

Xiangren Sun[1,2] | Jian Cao[1,2,3] | Ye Li[1,2,3] | Baoxu Wang[1,2]

[1]College of Shipbuilding Engineering, Harbin Engineering University, Harbin, China

[2]Science and Technology on Underwater Vehicle Technology Laboratory, Harbin Engineering University, Harbin, China

[3]Sanya Nanhai Innovation and Development Base, Harbin Engineering University, Sanya, China

Correspondence
Jian Cao and Ye Li, Harbin Engineering University, No.145 Nantong St, Harbin, Heilongjiang Province, China.
Email: caojian@hrbeu.edu.cn and liyeheu103@163.com

Funding information
The Hainan Provincial Joint Project of Sanya Yazhou Bay Science and Technology City, Grant/Award Number: 520LH007; The National Natural Science Foundation of China, Grant/Award Number: 52071104; The Stable Supporting Fund of Science and Technology on Underwater Vehicle Technology, Grant/Award Number: JCKYS2023SXJQR-02

Abstract

This paper presents the design and field test of a foldable wing unmanned aerial–underwater vehicle (UAUV). The vehicle can complete diving and air operations, and still have the ability of multiple trans-medium water egress and ingress under the condition of carrying mission load during a single flight. The wings can be folded back for drag reduction in underwater sailing and water egress, and unfolded to provide lift for flight after water egress. This paper presents the major components and system design of the vehicle, including the overall structure of the vehicle, the design of the mechanism for self-locking and quick-folding, the design of the electrical system, the selection of the propulsion system, and analyzes the performance gains from foldable wings and foldable propellers. Then the trans-medium field test was introduced, and the analysis and discussion were conducted for the four typical operating conditions of the vehicle, including water sailing, aerial flight, water egress and water ingress. Furthermore, the endurance performance under the corresponding operating conditions is estimated based on experimental data and the current battery energy carried. The presence of foldable wings and a large pitch angle water egress strategy reduces the thrust-to-weight ratio requirement for the vehicle. The results of the field tests can provide important experience and data support for the subsequent application-oriented UAUVs.

KEYWORDS
foldable propeller, foldable wing, unmanned aerial–underwater vehicle, water egress, water ingress

1 | INTRODUCTION

With the rapid accumulation of unmanned aerial vehicle (UAV) and unmanned underwater vehicle (UUV) technologies, there is an increasingly growing exploration in both the aerial and maritime domains. People's expectations for unmanned vehicles are no longer limited to the ability to operate under a single medium. In recent years, the unmanned aerial–underwater vehicle (UAUV) capable of underwater and aerial operations under a single cruise has received extensive attention from various research institutions. For example, researchers at Imperial College London have studied lightweight water-jet-powered UAUVs (Siddall & Kovac, 2017), Shanghai Jiao Tong University has designed UAUVs that can glide underwater and take off and land vertically (Lu et al., 2021), and North Carolina State University has designed a fixed-wing form of UAUV (Weisler et al., 2017). The UAUV combines the characteristics of UUVs and UAVs, with the invisible and low-energy cruising characteristics of UUVs and the fast maneuvering and long-range transmission capability of UAVs, making it adaptable to a wider range of application scenarios. For instance, the UAUV can be used for rapid multipoint sampling and investigation in various aquatic environments, deep-sea target detection and monitoring, early warning systems, and as a future mobile trans-medium

signal relay station to facilitate high-speed communication for underwater vehicles with the outside world (Yang et al., 2015).

Currently, there are two main research directions of the UAUVs: rotary-wing and fixed-wing (Tan & Chen, 2019a). The two modes of operation are different, but there are more common points in the trans-medium related technology can be referred to.

To address the problem of complex and variable disturbances during the water–air transition, Zha et al. proposed a strategy for a simple design of a quad-rotor UAUV, performed modeling and state estimation, and conducted experiments to validate the strategy and demonstrate its feasibility (Zha et al., 2019). Maia et al. developed a four-axis, eight-rotor trans-medium UAV with propellers in both water and air during the water–air transition, based on which they explored a seamless transition between air and water and advanced the study of a multimedium propulsion system for efficient water–air operation (Maia et al., 2017). Alzu'bi et al. proposed an unmanned hybrid aquatic–aerial quadcopter with active buoyancy control. They used a ballast system to control the buoyancy of the quadrotor underwater and thus change the depth, which provides a valuable idea and method for developing trans-medium vehicles (Alzu'bi et al., 2018). Tan et al. proposed a novel morphable design for a multirotor-based vehicle, presented the physical implementation of the concept and explored the physical design limitations of this new vehicle. The rotatable cantilever helps the vehicle achieve six degrees of freedom of movement underwater, which provides new ideas for underwater motion (Tan & Chen, 2019a). In addition, to address the problem of air propulsion system operating underwater, Tan et al. provide a motor-propeller matching evaluation and optimization method to design a water–air propulsion set, which can be better adapted to underwater and air environments (Tan & Chen, 2019b). Canelon-Suarez et al. proposed a universal trans-medium platform that adds a screwdrive drivetrain to a diveable quadrotor to achieve land and water propulsion and installs a pump to achieve control of vehicle lift and sink, thus enabling the vehicle to cope with different types of mission requirements, which is an inspiring solution to the difficult problem of performing tasks in complex environments (Canelon-Suarez et al., 2020). Li et al. proposed a quadrotor trans-medium vehicle with a hitchhiking device that not only seamlessly transitions between air flight and water sailing, but also can be attached to the surface of various objects to achieve hitchhiking. It opens up new possibilities for applications such as biomonitoring, surveillance, and long-time tracking (Li et al., 2022). Lu et al. demonstrated a hybrid aerial underwater vehicle with a wing mounted on a quadrotor fuselage, integrating an underwater glider, a quadrotor, and a fixed-wing vehicle. It uses a quad-rotor mode for low-speed takeoff and landing, a fixed-wing aircraft mode for high-speed flight in the air, and an underwater gliding mode for underwater operation with changing buoyancy. This new form of combining the advantages of different vehicles provides ideas for flexible and efficient mission execution (Lu et al., 2018, 2019, 2021; T. Wei, Lu, et al., 2022).

Rotary wing trans-medium vehicles have the capability to traverse different mediums through vertical take-off and landing, as well as hover in the air. These vehicles are particularly suitable for low-speed, short-range air missions. However, the performance of underwater rotary wing vehicles is limited by low speed, high energy consumption, relatively short endurance, and low maximum speed, making it difficult to quickly cover a wide range of mission areas. In addition, these vehicles require high stability control and are susceptible to external disturbances such as wind (Zeng et al., 2022).

In terms of fixed-wing UAUVs, Siddall et al. designed a device that uses high-pressure CO_2 water jets to generate thrust to assist the vehicle in water egress. Although the complete process of trans-medium tests could not be achieved, the studies provide important ideas for water egress and ingress modes of fixed-wing UAUV (Siddall & Kovač, 2014, 2015, 2017; Siddall et al., 2017). Zufferey et al. used a large amount of gas generated by a chemical reaction of solid reactants to achieve water jet propulsion and validated it on a miniature delta-wing prototype, which provides a promising solution for future high-power density trans-medium propulsion (Zufferey et al., 2019). Liang et al. made a detailed analysis of the load characteristics of the bionic folding wing vehicle under different states of water entry through design tests. And derived the relationship between the peak load at the root of the wing and the water entry height, swept-back angle and water entry angle, revealing the wing load characteristics for diving into water (Liang et al., 2014, 2013). The proposed amphibious UAV by Yang et al. performs a large pitch angle air–water transition by plunge-diving, which puts high demands on the structure and control stability of the vehicle, but this approach can achieve the water–air medium transition in a shorter time (Yang et al., 2013). Yao et al.'s submersible flying boat uses a seaplane-like takeoff and landing method, which is a successful way to explore fixed-wing vehicles across media, although the water-air transition is time consuming (Yao et al., 2014). Weisler et al. designed a fixed-wing UAUV capable of operating underwater and in the air, and conducted a full-scale field test in and out of the water to verify the feasibility of water–air transition for fixed-wing vehicles. But the relatively large wingspan inevitably increases the drag during underwater navigation and out of the water (Weisler et al., 2017). Stewart et al. conducted an experimental analysis of the problem of passive water drainage in the wing of fixed-wing UAUVs. They compared the advantages and disadvantages of different trans-medium vehicle operating modes and ultimately selected the VTOL tail-sitter aircraft concept for further development and testing. Their results provide a valuable design reference for fixed-wing UAUVs (Stewart et al., 2018, 2019). Wei et al. designed a delta-wing UAUV that weighs about 3 kg and has a lower density than water. The air propellers on the left and right sides of this vehicle are used for air and underwater propulsion, and it can be submerged from the surface by means of elevator. The paper presents the relevant experiments and summarizes the motion characteristics of this type of dual-propulsion vehicle

(Z. Wei, Teng, et al., 2022). Rockenbauer et al. developed a 3.1 kg lightweight foldable wing UAUV and designed a dual-use air–water propulsion system to achieve trans-medium access in the simplest possible design and manufacturing form. However, due to the low weight and working depth of the UAUV, its duration of operation and payload capacity are severely restricted, resulting in challenges for mission application (Rockenbauer et al., 2021).

Compared to rotary-wing UAUVs, fixed-wing UAUVs typically have more streamlined fuselages, making them better suited for underwater cruising. With the ability to achieve higher flight speeds and longer ranges under similar conditions, they have great potential for further development (Farinha et al., 2021). However, fixed-wing UAUVs have fewer propellers to provide thrust, making their attitudes more prone to instability, while their ability to exit the water is also more challenging.

Currently, research on fixed-wing UAUVs has not yet achieved the large dive depth, long range, and large payload capabilities that researchers expect. Moreover, most vehicles lack the ability to repeatedly enter and exit the water during a single voyage. However, there are obvious prospects for the development of fixed-wing UAUVs.

This paper proposes a design scheme for a fixed-wing UAUV with foldable wings to address the challenges of high resistance during underwater sailing and strong impact during water entry. The scheme aims to maximize both underwater cruising and air flight performance while reducing the thrust-to-weight ratio requirement of the UAUV. This is achieved by folding the wing to reduce drag and utilizing a high-pitch angle control mode when the UAUV is exiting the water. Thus the requirement for the thruster and the power consumption of the trans-medium process will be reduced. This article will conduct various operational tests and performance evaluations to validate the designed trans-medium vehicle, aiming to increase the diving depth and payload capacity of the fixed-wing UAUV to practical levels and equip it with preliminary engineering application capabilities.

2 | SYSTEM OVERVIEW OF THE FOLDABLE WING UAUV

This paper proposes a fixed-wing UAUV prototype "Longbow II" (LB-II) with foldable wings, which can not only navigate smoothly in water and air, but also to realize the transition of the medium from the underwater to the air and from the air to the underwater. According to Figure 1, LB-II can be deployed on land or on a surface platform such as a ship, hand launching and arresting net landing can be utilized in narrow areas (Kim et al., 2013; Skulstad et al., 2015). LB-II has four operating states: water sailing, aerial flight, water egress and water ingress. It can play a significant role in rapid sampling of the marine environment, maritime reconnaissance and monitoring, and underwater-air inter-medium communication relay. Based on the above application requirements, the designed LB-II needs to be able to complete multiple water egress and water ingress operations under the same voyage, designed for a maximum operating depth of 100 m, and has the ability to carry various sensors and other mission loads.

2.1 | General design

Due to the requirement for LB-II to operate in two vastly different fluids, water and air, the design process has to consider its flight performance, such as generating enough lift to counteract gravity during flight, as well as its stability for underwater sailing. Additionally, it is important to have a light, low-resistance fuselage and strong power to enable LB-II to achieve the medium conversion

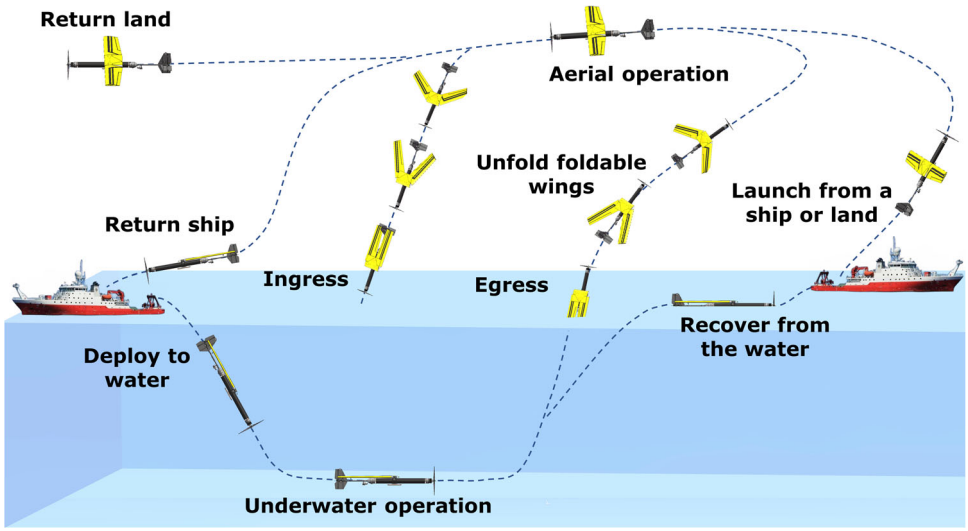

FIGURE 1 Multiple operation modes of Longbow II.

from water to air. Moreover, the fuselage needs to be strong enough to prevent structural damage when entering the water, making the LB-II design more challenging.

2.1.1 | Main scale and configurations

As a fixed-wing UAUV, LB-II has a fuselage length of 1.95 m, a wingspan of 2.535 m, and a weight of 13.3 kg (including a 995 g conductivity-temperature-depth sensor [CTD]) as shown in Figure 2 LB-II is equipped with foldable wings that can be folded backwards. The wings are folded during underwater sailing and the process of crossing the medium from water to air, reducing the frontal area of the fuselage. This significantly reduces the drag during underwater sailing and when leaving the water. Moreover, it can also reduce the impact when entering the water, which is crucial for UAUV to successfully complete the trans-medium mission. Detailed computational analysis is presented in Section 2.5.

LB-II adopts lightweight design, with the main fuselage structure made of high-strength carbon fiber material. Some of the frame structures have been hollowed out without affecting the strength of the main body. LB-II has an upper monoplane configuration, with a carbon fiber pressure-resistant cabin installed at the bottom of the wing as the main part of the fuselage. The front cover of the cabin is installed with a motor and a propeller for air propulsion, and the rear cover is installed with carbon fiber rods for connecting the tail. The cross-shaped tail features a rudder and elevator for adjusting the yaw and pitch of the LB-II, respectively. A thin fairing shell is used to wrap the conductors and some fixed structures in the front and rear end caps of the pressure-resistant cabin to reduce the resistance to sailing.

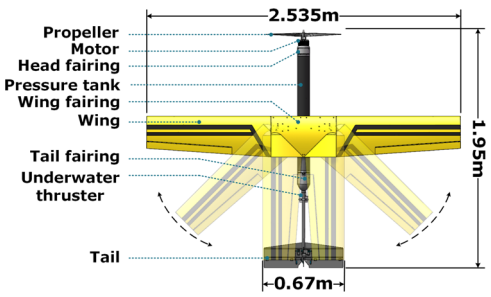

FIGURE 2 Main scale and composition of Longbow II.

A small camera is mounted inside the rear end cap fairing shell to transmit the captured images back to the ground station in real time. An underwater thruster is mounted underneath the carbon fiber rod behind the rear end cap fairing to provide a maximum of approximately 5.0 kgf of underwater static propulsion for the LB-II.

2.1.2 | Wing structure

As shown in Figure 2, LB-II has a pair of trapezoidal wings with a chord length of 0.33 m at the wing root and 0.29 m at the wing tip, and a single wing length of 1.005 m, with a spreading chord ratio of 8.6 when both sides are fully expanded. The trailing edge of the wing is equipped with an aileron near the wing tip for adjusting the attitude of LB-II in the cross-roll direction. Before landing, the aileron can be deflected downward and used as a flap, which can increase the wing curvature to improve the lift and drag, thus reducing the landing approach speed.

Under the same conditions, a larger wing area may provide more lift, and a larger chord ratio may reduce induced drag and improve the lift-to-drag ratio during flight, thereby improving the aerodynamic efficiency of the flight. Another important point is that the trapezoidal wing has low processing difficulty, low induced drag, and its stable and reliable performance is very suitable for application in a new type of vehicle such as the LB-II.

The wings are machined from carbon fiber material, with a thin carbon fiber shell on the outer surface and a hollow structure inside, and is structurally reinforced by carbon fiber ribs and crossbeams, as shown in Figure 3. To realize lightweight design and facilitate the rapid flow of water in and out of the wings, the internal ribs and crossbeams are equipped with numerous relief holes while ensuring strength. The leading edge of the wing up to the crossbeam is filled with buoyant material that can withstand a pressure depth of 100 m, which provides partial buoyancy for LB-II when working underwater on the one hand, and the solid filling inside the wing improves the torsional and bending resistance of the wing on the other hand. Two carbon fiber tubes are installed at the wing root for connection with the wing folding mechanism.

A carbon fiber frame serves as the connection structure between the wings and the fuselage, while the wing folding mechanism is mounted on both ends of the carbon fiber frame. Carbon fiber fairing shells are used to cover both wings and reduce drag.

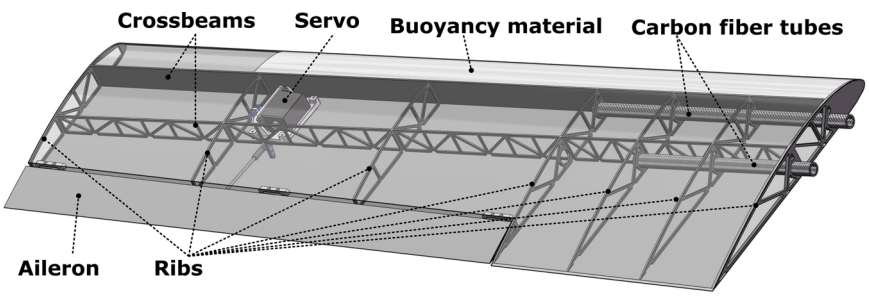

FIGURE 3 Composition of the wing structure.

2.1.3 | Pressure-resistant cabin

LB-II's carbon fiber pressure-resistant cabin has an outside diameter of 100 mm, and aluminum alloy hatch covers are installed at both ends of the cabin, with O-rings used to complete the seal between the cabin and the hatch covers. The pressure-resistant cabin is mainly used to install some water-sensitive electronic devices such as batteries. Figure 4 shows the pressure test results of the cabin, which was tested up to 1.424 MPa, equivalent to a water depth of approximately 145 m.

2.1.4 | Control surfaces

To simplify the tail machining difficulties and avoid the excessive tail drainage volume to significantly affect the floating center position, the cross-shaped tail stabilizer and rudder surfaces are cut directly from thin carbon fiber sheets. And carbon fiber reinforcement strips are attached to the surface of the tailplane to improve the ability of the carbon fiber sheets to resist bending and torsional deformation. The tailplane, carbon fiber reinforcement strips and carbon fiber tail rod are embedded and bonded to each other, and finally installed on the rear end cover of the pressure-resistant cabin.

Similar to a conventional fixed-wing UAV, the LB-II controls attitude through a total of five maneuvering surfaces: left and right ailerons, left and right elevators and a rudder, as shown in Figure 5. The left and right deflection of the rudder is used to adjust the LB-II heading. The left and right ailerons are deflected in opposite directions to create a roll moment around the fuselage axis to control the roll attitude, and the left and right ailerons are deflected downward at the same time to increase the curvature of the wing surface and act as flaps, which can be opened during landing to increase the lift and reduce the airspeed. In the folded state, the aileron axis is almost parallel to the longitudinal axis of the fuselage, so it no longer has the role of adjusting the roll attitude. The elevator also consists of two control surfaces, the left and right control surfaces are deflected up and down simultaneously to adjust the pitch angle of the LB-II when the wings are deployed. In the folded state, the elevators not only need to adjust the pitch angle, but also take into account the role of fine-tuning the roll angle. To adjust the roll angle in this state, the left and right control surfaces deflect at different angles, creating a roll moment. However, due to the small distance between the control surfaces, the roll angle adjustment is limited, as shown in Figure 6.

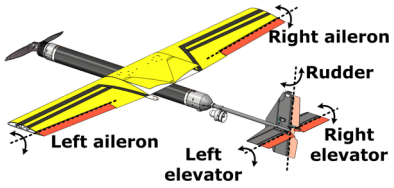

FIGURE 5 The control surfaces of Longbow II.

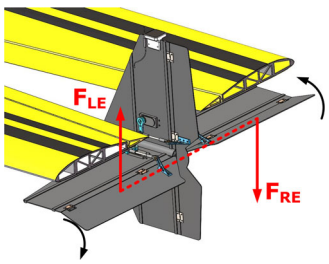

FIGURE 6 Left and right elevator surfaces reverse deflection.

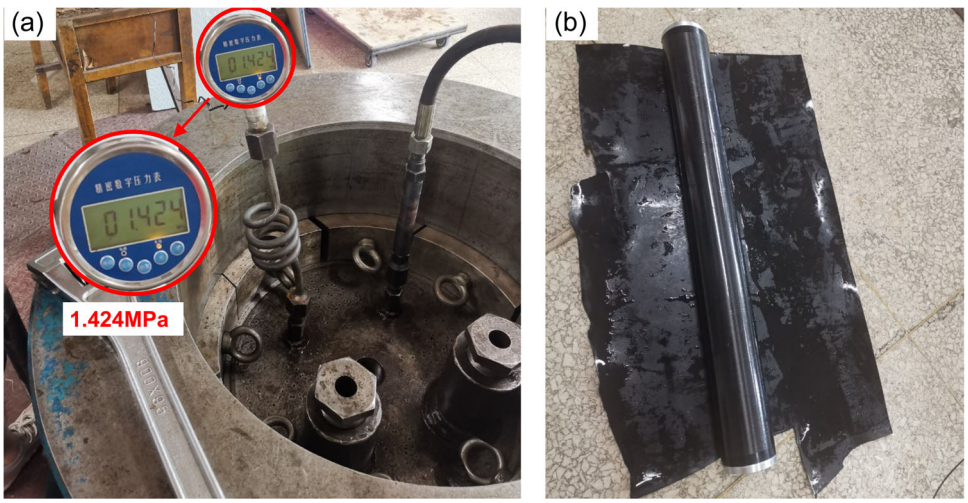

FIGURE 4 Carbon fiber pressure-resistant cabin pressure test. (a) The pressurization process of the pressure-resistant cabin, and the pressurization tank shows a pressure of 1.424 MPa. (b) The pressure-resistant cabin at the end of the pressurization.

2.1.5 | Gravity and buoyancy in water

The LB-II has a net buoyancy of approximately 0.8 kgf, which provides slight positive buoyancy. This allows the LB-II to move smoothly underwater without requiring excessive intervention, and also enables it to resurface easily in the event of an underwater accident.

The LB-II is always deployed with the wings in the air. The center of gravity is designed to be located aft of the leading edge of the wing, positioned at 25% of the average aerodynamic chord length from the leading edge. The center of gravity and the center of buoyancy are on the same plumb line, and the center of buoyancy is directly above the center of gravity, as shown in Figure 7. Its center of gravity and center of buoyancy should meet the different requirements of air navigation and underwater navigation simultaneously.

2.2 | Folding mechanism design

The key to the folding capability of the LB-II wings is the wing folding mechanism, which can push the wings to achieve a 90° rotation, that is, unfold perpendicular to the longitudinal axis of the fuselage, or fold parallel to the longitudinal axis of the fuselage as shown in Figure 2. The mechanism is self-locking in the fully extended and fully retracted positions to maintain a constant wing angle without the need for continuous servo power. The main components of the folding mechanism include the rotatable wing connector, chute, slider, connecting rod, shaft, servo and servo rocker arm.

As illustrated in Figure 8, the servo output shaft is fixed to the servo rocker arm. One end of the connecting rod is attached to the servo rocker arm, and the other end is connected to the slider. The end of the slider slides in the chute, while the central rod part of the slider pushes the wing connector to rotate. The wing connector is fixed to the wing.

As shown in Figure 9, when the servo rotates counterclockwise, the slider moves to the left along the chute. This causes the wing connector to also rotate counterclockwise. The angle of the line between the center of the slider and the center of the shaft axis (orange dashed line) remains unchanged as the slider passes through the inflection point. Once the wing connector stops rotating, the wing will reach a folded position parallel to the longitudinal axis of the fuselage. However, under the continuous push of the servo, the slider will continue to slide along the chute to the upper left end point. At this point, when the wing is subjected to an external disturbance torque and the wing connector has a tendency to rotate around the axis, the direction of the force on the slider is perpendicular to the line connecting the slider axis and the axis of the shaft (orange dashed line). And the slider is stuck to the chute, thus realizing the self-locking of the mechanism. When the wing needs to deploy, the servo turns in the opposite direction, and the principle is exactly the same as when the wing is folded.

The advantage of the folding mechanism is that it can be self-locking in the folded or unfolded state, consuming less energy and folding faster. Once the folding mechanism has reached the folded or unfolded state, it does not require continuous power to the servo to lock. The servo will be powered down for 3 s and then powered up for 1 s to ensure that the mechanism is securely locked, and so on until a new motion command is received. With the folding mechanism locked, this measure reduces the servo's operating time to only 25% of its original duration, while maintaining the same level of functionality. As a result, the energy consumption of the servo is significantly reduced. To achieve a quick deployment when leaving the water, the servo power in the direction of the wings deployment is set to the highest level, and since the maximum speed is not needed to fold the wings when entering the water, the servo folding process is set to a medium torque level to save energy.

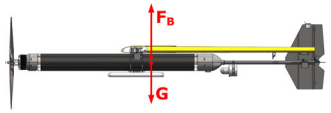

FIGURE 7 Schematic diagram of Longbow II's gravity and buoyancy in water.

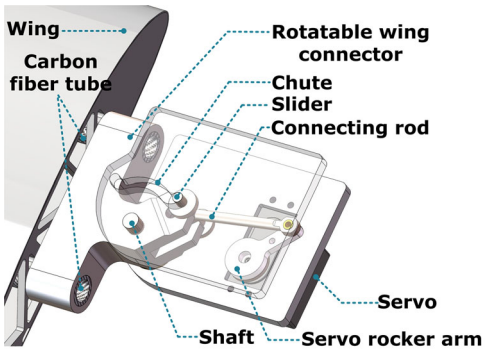

FIGURE 8 Composition of the folding mechanism.

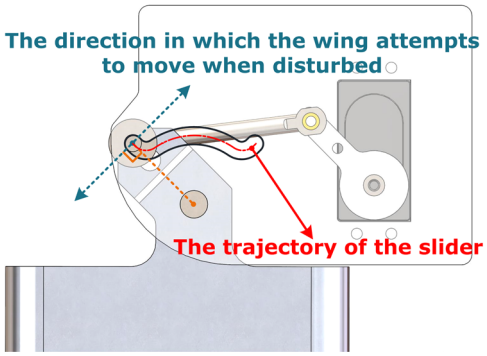

FIGURE 9 The folding mechanism slider movement.

The folding mechanism of the installed wings was tested and the results showed that the wings took only about 0.6 s from folding to unfolding and about 1.1 s from unfolding to folding. The fast and low energy consumption folding mechanism is the core mechanism of the LB-II, which ensures that the LB-II can smoothly and quickly complete the mode change over the trans-medium process.

2.3 | Electrical system

Figure 10 shows the electrical system relationship of LB-II, the main electrical equipment on board LB-II includes a 12S main battery, a backup battery, power modules, a current sensor, an ultra battery elimination circuit (UBEC), electronic speed controllers (ESC), servos, thrusters, a

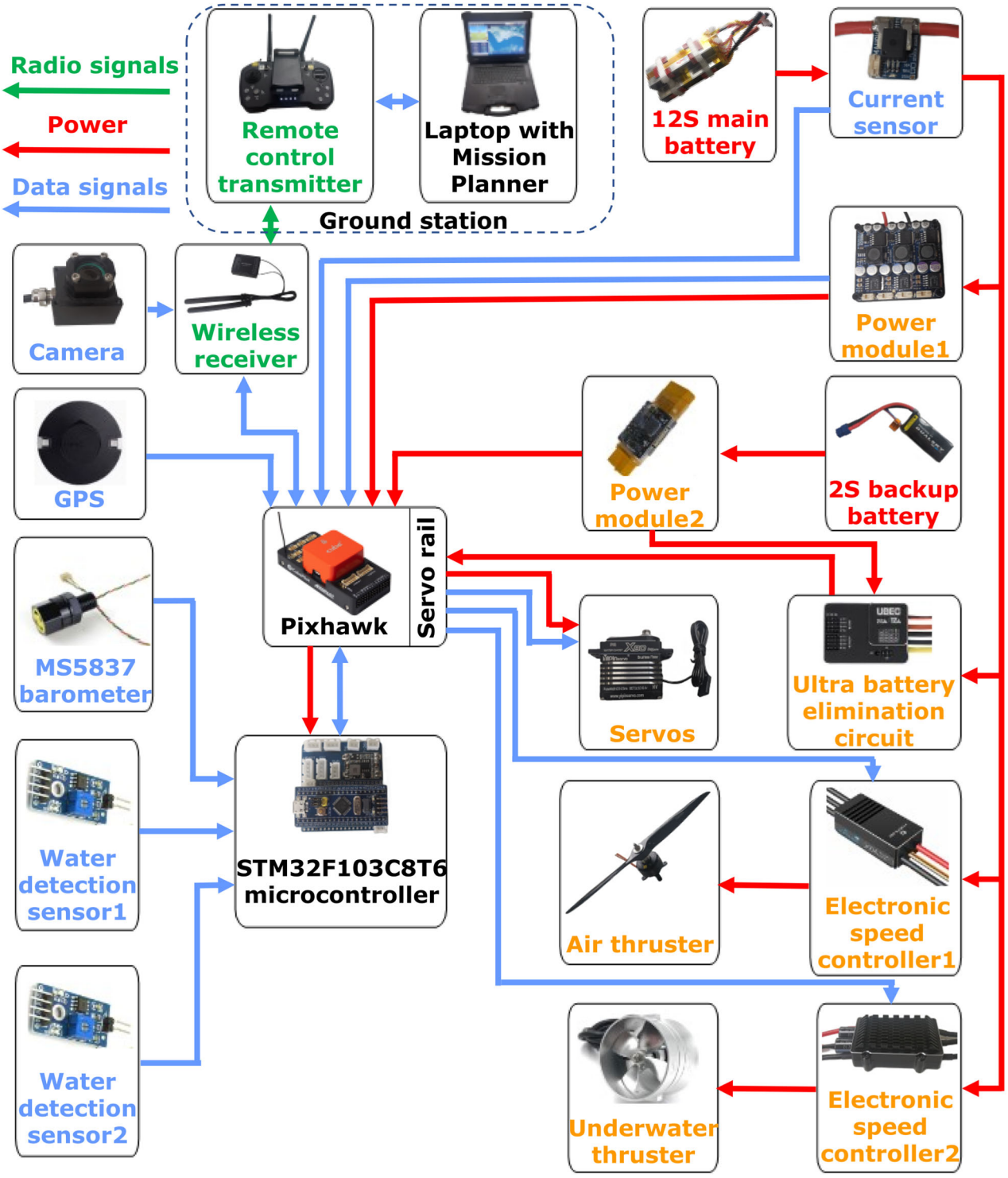

FIGURE 10 Electrical system connection diagram, where the red text represents the power supply, black represents the control unit, blue represents the sensors, green represents the communication equipment, and orange represents other electrical equipment.

Pixhawk autopilot, a STM32F103C8T6 microcontroller, an MS5837 barometer, water detection sensors, a camera, and a GPS module. The ground equipment consists mainly of a laptop with a mission planner and a remote control transmitter.

As an autopilot, the Pixhawk is one of the LB-II's most central devices, responsible for controlling the LB-II's operating attitude, performing prescribed flight tasks, and recording important flight data. Since the Pixhawk was installed in the enclosed space of the pressure-resistant cabin, the barometer could not measure the outside air pressure, so an MS5837 barometer was installed outside the pressure-resistant cabin to measure the air and water pressure, from which the height or depth at which the LB-II was located could be calculated. In addition, to accurately detect the medium environment in which the LB-II is located, we installed two water detection sensors, whose detection modules are installed in the pressure-resistant cabin. The detection points are located on the front rectifier shell and the tail surface, respectively, to determine whether the LB-II's head and tail are in water or air by detecting the presence or absence of water at these points. Data from the MS5837 barometer and water detection sensors is collected by the STM32 microcontroller, and the results are transmitted to the Pixhawk flight controller through the serial port. Finally, the Pixhawk flight controller makes a comprehensive assessment of the aircraft's condition and makes appropriate decisions.

The 12S Li-ion battery is the primary power source for the LB-II, with a total capacity of approximately 284.2 Wh. The current flows through a current sensor and power is supplied to an UBEC, two ESCs, and a power module with voltage measurement and 5 V power supply capability that powers the Pixhawk flight controller. The UBEC receives high voltage and outputs low voltage matched to the Pixhawk servo rail, allowing the servos connected to the Pixhawk servo rail to receive power and signals directly from the Pixhawk.

The two ESCs receive signals from the Pixhawk and power from the main battery to drive the air thruster and the underwater thruster, respectively. The 2 S backup lithium battery will not function under normal circumstances and will only power the UBEC and Pixhawk via the power module in the event of a disconnect in the main battery circuit. In this extreme case of main power failure, the LB-II's thrusters will not work, but the Pixhawk and servos can be maintained through the backup battery. If the LB-II is in the air at the time of the power failure, the ground side can still maintain communication with the LB-II, communication can still be maintained with the ground, and the LB-II can attempt to maintain its landing attitude through servo maneuvers. If the LB-II is underwater at the time of the power failure, it will rely on positive buoyancy to slowly rise to the surface and establish communication with the ground.

The ground side of the LB-II uses the Mission Planner software to monitor the LB-II's operating status in real time and to perform parameter adjustments and mission planning. The ground laptop is connected to the remote control via the data cable. When the LB-II receiving antenna is in the air, the remote control can be used as remote control, telemetry transmission and video transmission, which can send parameters, mission commands and remote control signals to the LB-II, and also receive all kinds of status information returned from the LB-II and real-time images captured by the camera.

Based on the original flight mode of the Pixhawk flight controller, the LB-II adds two operating modes for different scenarios, including underwater sailing mode and water egress mode. Underwater mode is used for long-range underwater navigation for the LB-II since it cannot communicate with the outside world underwater. It can only maintain heading and depth using inertial elements like the IMU and barometer.

Due to the limited accuracy of these inertial elements, the LB-II must surface after a period of underwater navigation to calibrate its heading and position via GPS, and then dive to continue navigation to the next target waypoint. The water egress mode can be activated at the surface or underwater. Once activated, the LB-II will automatically set the depth and pitch angle to exit the water. After water egress, it can automatically switch to waypoint flight mode to complete the waypoint task and land on the water surface by itself according to the task setting, or it can automatically switch to circle mode and remain airborne, waiting for the pilot to intervene by remote control.

2.4 | Propulsion system

The LB-II airborne propulsion system consists of a brushless motor with a peak power of about 6000 W, a matching ESC, and a propeller. Two types of propellers are available: a two-blade 24-inch propeller that can provide a maximum thrust of approximately 19.9 kgf, resulting in an overall thrust-to-weight ratio of 1.49, and a two-blade 25-inch foldable propeller that can provide a maximum thrust of approximately 17.3 kgf, resulting in a thrust-to-weight ratio of 1.30. The physical diagram of the thruster is shown in Figure 11. A test facility for static thrust testing in air and underwater has been designed for the thruster, the principle of which is shown in Figure 12. Rod 1 and Rod 2 are rigidly connected, perpendicular to each other and rotating around the shaft, $l_1 = l_2$, so that the propeller thrust F_1 is equal to the tensile force of the tension meter F_2. The test results for the 24-in nonfolding propeller, the 25-in foldable propeller in the air thrust test, and the 24-in propeller in the water test are presented in Figure 13.

Based on the results, it can be observed that the thrust generated by the 24-in nonfolding propeller is consistently higher than that of the foldable propeller across all power levels. This difference can be attributed to differences in blade shape and the level of propeller matching. Therefore, if one aims to maximize air propulsion efficiency and water egress success rate, it is advisable to use the nonfolding propeller. However, if reducing underwater resistance is a priority, the foldable propeller can be considered as an option.

One option for underwater propulsion is to use the air thruster directly for underwater propulsion with smaller throttles to prevent damage to motors and ESCs from the high currents generated by large-diameter propellers operating underwater, which can reduce the complexity of the propulsion system and the system weight. In this paper, the selected motor with 24-in two-blade air propeller was tested underwater, the results are presented in Figure 14 and the test photos are shown in Figure 15. When the throttle is increased, the current curve rises with a large slope. Combined with the test site, the motor rotation is unstable when the throttle is lower than 12.5%, and the phenomenon of

FIGURE 11 Different forms of air thrusters. (a) The 24 inch nonfolding propeller, (b) the 25 inch foldable propeller, and (c) the folded state of 25 in foldable propeller.

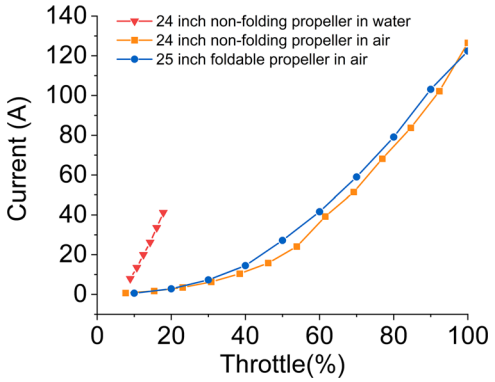

FIGURE 14 Throttle-current curve for propeller static thrust test.

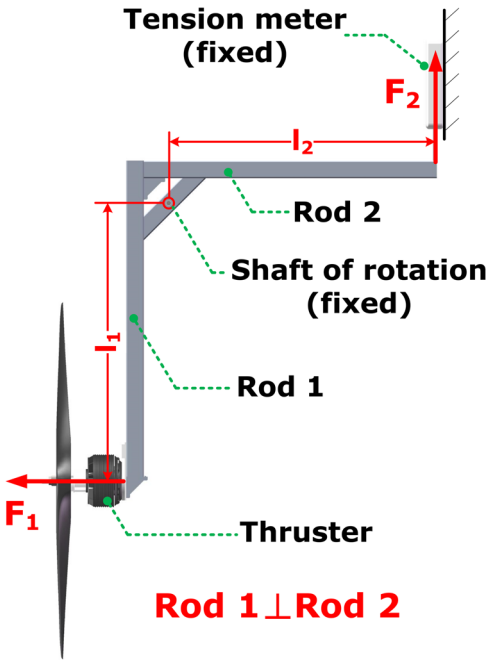

FIGURE 12 Schematic of the static thrust test facility, where $l_1 = l_2$, $F_1 = F_2$.

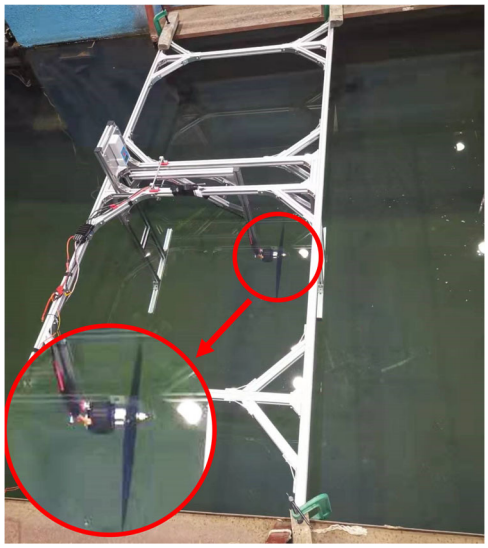

FIGURE 15 Thrust test of air propeller in water.

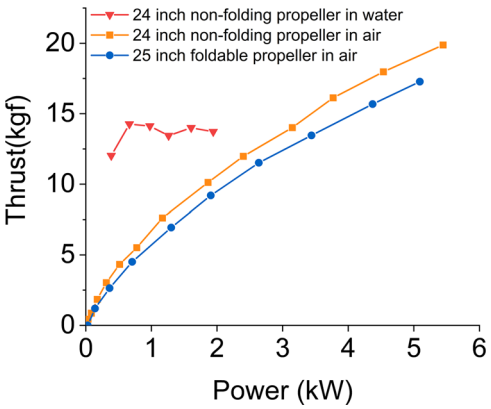

FIGURE 13 Power-thrust curve for propeller static thrust test.

blocking and shaking caused by excessive rotational resistance appears. This is due to the fact that the large diameter propeller used directly for underwater propulsion requires a higher motor torque, and the torque is already approaching the limit when the motor is driving the 24-in propeller to achieve a smooth rotation during the test. As a result, increasing the throttle further will only increase the current and create thermal effects.

The results of underwater propulsion tests conducted by Wei et al. for air propellers showed that the propulsion efficiency of air propellers operating underwater was lower than that in air, and the tests in this paper yielded different results as shown in Figure 14 (Z. Wei, Teng, et al., 2022). This may be due to the different motor-propeller matching. The 24-in propeller selected for the LB-II was specifically chosen to maximize air propeller performance for higher thrust, therefore, for underwater propulsion, it has a larger diameter and operates more efficiently underwater (Carlton, 2019). In summary, using the air propeller directly underwater results in high

power consumption, limited adjustable speed range, unstable speeds, and generates excessive heat in the ESC during underwater propulsion, which may affect subsequent full-throttle high power output when exiting the water. Therefore, the selected air propeller for LB-II is not suitable for underwater operation.

Rockenbauer et al. designed a reduction gear for high speed brushless motors, which opens and closes a clutch to drive an air or underwater propeller, respectively (Rockenbauer et al., 2021). Tan et al. also designed a reduction gearbox for air propellers to meet both underwater and air propulsion requirements (Tan et al., 2017). However, due to the LB-II air propeller's higher peak power, the corresponding gearbox or clutch system would be larger and heavier, and the more complex mechanical structure would increase the potential for reliability issues. Therefore, this solution was not pursued.

The final underwater propulsion solution for LB-II uses a dedicated thruster designed for underwater use, with a diameter of 71 mm and a maximum power output of about 450 W, capable of generating a maximum thrust of about 5.0 kgf. The total weight of the underwater thruster and the corresponding ESC is about 398 g, which means that the weight of the thruster must be carried at all times during flight. However, the weight of the thruster is relatively small compared to the total weight of the vehicle. Importantly, the adjustable speed range of the underwater thruster is wide and its energy consumption is significantly lower than that of the air thruster when working directly underwater, fully meeting the underwater propulsion requirements of the LB-II.

2.5 | Discussion of the effects of foldable wings and foldable propellers on performance

This section briefly analyzes and calculates the performance enhancement of the LB-II by foldable wings and foldable propellers.

2.5.1 | Effects on underwater sailing

An important reason for the LB-II's use of foldable wings and foldable propellers is that this form of construction significantly reduces the resistance when underwater. For underwater vehicles, navigation resistance can be divided into frictional resistance and viscous pressure resistance according to the causes (Molland et al., 2017). The former is mainly related to the wet surface area of the vehicle and the latter is mainly related to the shape of the vehicle under the same state of navigation. The presence of conventional nonfolding wings and the nonfolding propeller increases the cross-sectional area perpendicular to the direction of the incoming flow when the vehicle sailing in the water. In particular, the nonfolding air propeller acts as an attachment to the fuselage, and the nonstreamlined characteristics of its rear end lead to drastic changes in flow velocity and pressure, which can cause a marked increase in viscous pressure drag. Therefore, the foldable wings and foldable propellers can help the LB-II to reduce the viscous pressure drag when sailing.

To deeply analyze the effects of foldable wings and foldable propellers on the underwater navigation of LB-II, this paper utilizes the computational fluid dynamics (CFD) software STAR-CCM+ to analyze the drag components of the underwater navigation of LB-II installed with different propellers and different states of wings.

The hydrodynamic calculation adopts the same three-dimensional model as the actual size of LB-II, and the model is moderately simplified before the calculation. The model deletes some small structures that have little influence on the hydrodynamics, but keeps the structures that have significant influence on the hydrodynamics, such as the air propeller, the permeable fairing shell, the hollow wings and the main structural frame, and so on. The four models of LB-II, folded and unfolded wings, the foldable propeller and nonfolding propeller, are faced with 1 m/s water flow in the flow field to calculate the navigational resistance, and the meshes are divided as shown in Figure 16 below. The model cases and the corresponding calculation results are shown in Table 1.

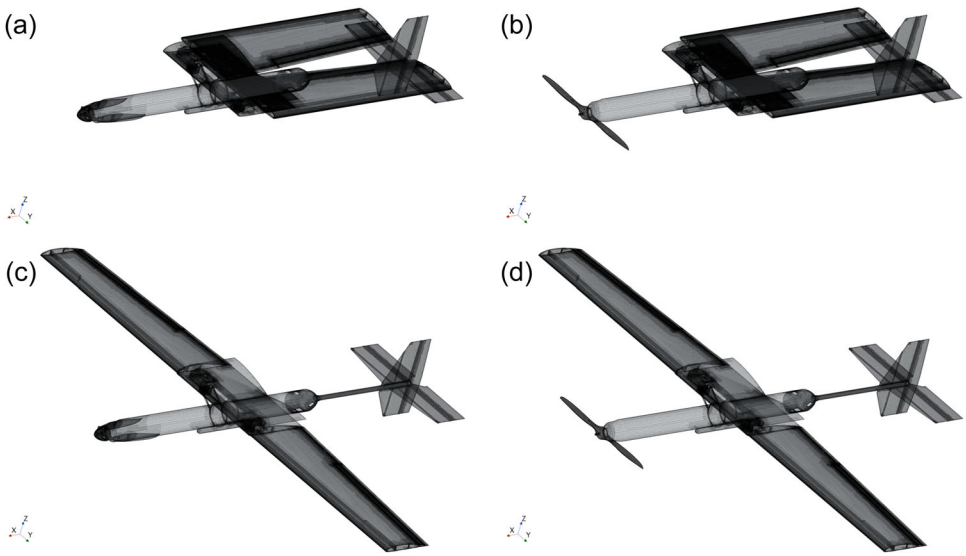

FIGURE 16 Schematic diagram of Longbow II meshing, where (a) is folded wings with a foldable propeller installed, (b) is folded wings with a nonfolding propeller installed, (c) is unfolded wings with a foldable propeller installed, and (d) is unfolded wings with a nonfolding propeller installed.

TABLE 1 Calculation results of different structural forms of LB-II at 1 m/s in CFD software.

Wing	Air propeller	Frictional resistance (kgf)	Viscous pressure resistance (kgf)	Total resistance (kgf)
Folded	Folded	0.504	1.418	1.922
Folded	Nonfolding	0.500	2.399	2.899
Nonfolding	Folded	0.560	1.710	2.270
Nonfolding	Nonfolding	0.554	2.729	3.283

According to the data in the table, the existence of folded wings and the folded propeller will considerably reduce the resistance of the LB-II in underwater sailing. In the case of underwater sailing with folded wings, the use of the folded propeller reduces the sailing resistance by about 33.7% compared to the use of the nonfolding propeller. In the case of both folded propellers, the folded wings reduce the sailing resistance by about 15.3% compared to the nonfolding wings.

Comparison of LB-II resistance values for different structural forms is shown in Figure 17. The figure shows that the frictional resistance of different structural forms of LB-II is almost the same when sailing straight underwater. The main cause of the difference in resistance is the viscous pressure resistance. Figure 18 shows the pressure distribution of different configurations of wings and propellers during underwater navigation, where red to blue colors represent the pressure from high to low. In Figure 18b, there are obvious pressure changes at the front and rear ends of the nonfolding wings and the nonfolding propeller, while the magnitude and range of the pressure changes in the corresponding regions in Figure 18a are reduced. Changes in pressure cause changes in the flow field, resulting in an increase in viscous pressure drag, which is the primary reason for the high drag of nonfolding wings and nonfolding propellers.

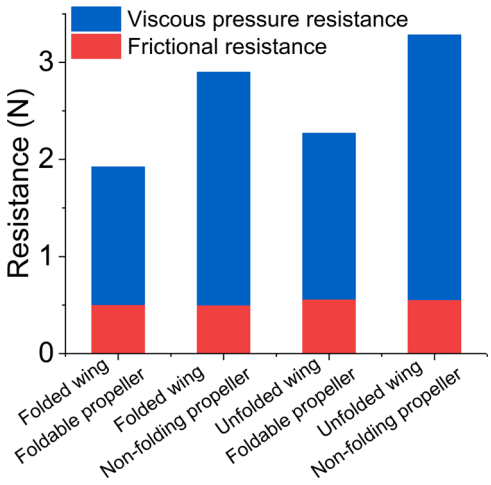

FIGURE 17 Comparison of resistance values of Longbow II with different structural forms.

2.5.2 | Effects on aerial flight

Compared to the conventional fixed wing configuration, the presence of the wing folding mechanism increases the weight of the LB-II by approximately 0.946 kg at the same structural strength, including all parts of the folding mechanism located between the two wings, as shown in Table 2. The weight of the folding mechanism would make the LB-II a little less maneuverable, and the gravity-lift balance would require higher speeds to achieve, and have an impact on endurance.

The flight speed of the LB-II in the gravity-lift balance was calculated by STAR-CCM+, which is similar to the underwater drag calculations, and the LB-II wings are nonfolding. The results show that the flight speed of the LB-II is 32.6 m/s when the lift reaches 12.354 kgf and 33.8 m/s when the lift reaches 13.3 kgf, so the weight of the folding mechanism has less effect on the flight speed.

Assuming the LB-II is designed as a conventional fixed-wing UAV without a folding mechanism. Under the condition that all other factors remain the same, the weight reduction resulting from the elimination of the folding mechanism would be fully allocated to the increase in battery capacity. Based on the current energy density of the battery (162.4 Wh/kg), the estimated increase in energy capacity would be approximately 153.6 Wh. To account for the total power consumption of the control electronics and propulsion system during LB-II operation, the average power consumption was estimated based on several actual flight data points from Table 5 in Section 3.2. The average power consumption during flight was determined to be 1337.6 W. Consequently, with the increased battery capacity, the airborne flight time could be extended by approximately 6.9 min. This suggests that the weight of the folding mechanism reduces the potential for increasing the range of the vehicle. However, the above estimates do not account for the weight of the battery pressurization structure or the pressure-resistant cabin in which the batteries are housed, and in practice it is necessary to consider issues such as whether there is enough space left in the pressure-resistant cabin to accommodate additional batteries.

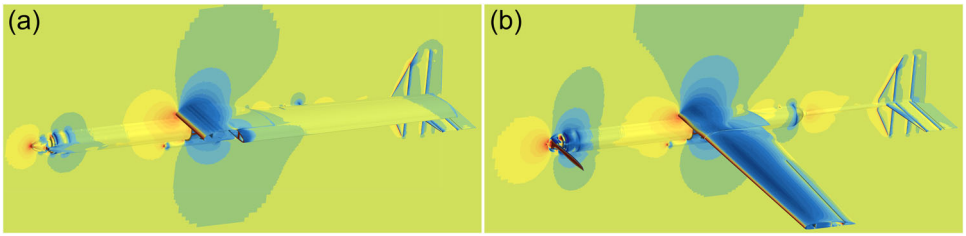

FIGURE 18 Pressure distribution images of the Longbow II during underwater navigation, where (a) is folded wings paired with a folded propeller, and (b) is unfolded wings paired with a nonfolding propeller.

TABLE 2 Weight statistics of folding mechanism parts.

Part name	Weights (kg)	Quantity (pcs/set)	Total weight (kg)
Servo	0.220	2	0.440
Rotatable wing connector	0.097	2	0.194
Chute	0.085	2	0.170
Connecting rod and other transmission structures	0.071	2	0.142
Total	/	/	0.946

2.5.3 | Effects on water egress

From the perspective of the impact on the take-off out of the water, under the same conditions, the installation of the folding mechanism will increase the weight of the vehicle, thus reducing the thrust-to-weight ratio, and causing certain difficulties in the water egress process. However, folding the wings reduces the resistance to water egress and helps water attached to the fuselage to drain quickly from the bottom wingtips, so the effect of foldable wings on water egress is more complex. In the following, the two forms of LB-II folded wings and nonfolding wings out of water are simulated by CFD means respectively and analyzed comparatively.

The virtual flow field is established in STAR-CCM+, with the upper half in air and the lower half in water, and the LB-II is initially positioned with the thruster just close to the water surface, with an initial velocity of 0 m/s and an initial pitch angle of 80°. To simplify the calculations, the motion of the vehicle is restricted to three degrees of freedom, that is, rotation and translation in the vertical plane only. The rotation of the propeller was simplified to a constant thrust of 17.3 kgf. The mass of LB-II with folded wings is 13.3 kg and the mass of LB-II with nonfolding wings is 12.354 kg. The computed images of the water egress are shown in Figures 19 and 20, the image of the egress instant is shown in Figure 21, and the change in vertical velocity throughout the process is shown in Figure 22. A combination of several data analyses shows that the folding wing version of the LB-II can achieve higher water egress speeds, and the water inside the hollow wings can be quickly drained from the wingtip, allowing the vehicle to successfully leave the water surface. The nonfoldable wing version of the LB-II cannot exit the water due to the higher wing drag. After the fuselage is partially out of the water, the upward force is not enough to overcome the drag and gravity.

2.5.4 | Effects on water ingress

To understand the water entry loads of the LB-II in both foldable and nonfoldable wing forms, a simplified model of the LB-II is placed above the water surface in the virtual flow field domain in STAR-CCM+ and is dropped by gravity to the water at a given initial velocity and initial pitch angle. The initial motion speed was set to 15 m/s horizontally and 3 m/s vertically, and the initial pitch angle was 10° with the nose down. The image of the instant of water ingress is shown in Figure 23. The force on LB-II is shown in Figure 24 and Figure 25, axial forces are positive in the forward direction, vertical forces are positive in the upward direction.

Based on the calculation results, the impacts suffered by the two models under the same conditions of water ingress are analyzed. At the moment of water entry, the maximum force on the folded wings of the LB-II is smaller than that on the unfolded wings, both axially and vertically. This indicates that the foldable wing design of the LB-II is effective in minimizing impact under the same water ingress conditions.

Comprehensive analysis results in this section show that the existence of folded wings and folded propellers of LB-II can

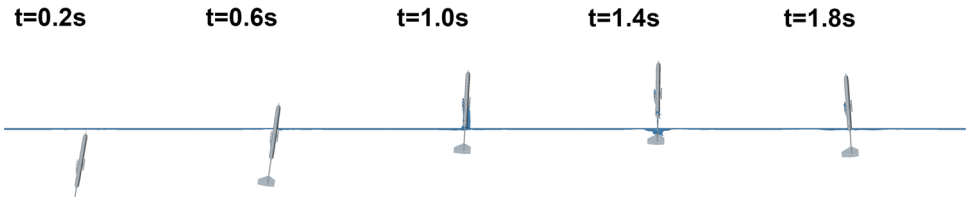

FIGURE 19 Computational fluid dynamic simulation image of Longbow II exit the water with nonfolding wings.

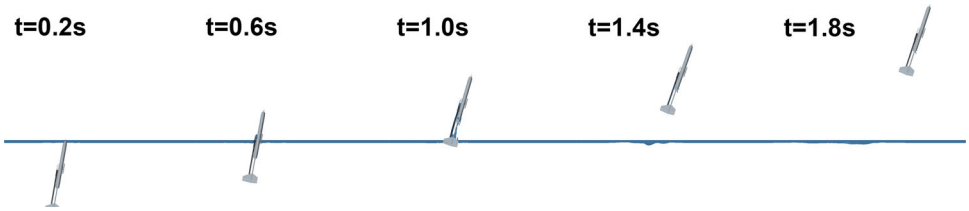

FIGURE 20 Computational fluid dynamic simulation image of Longbow II exit the water with folded wings.

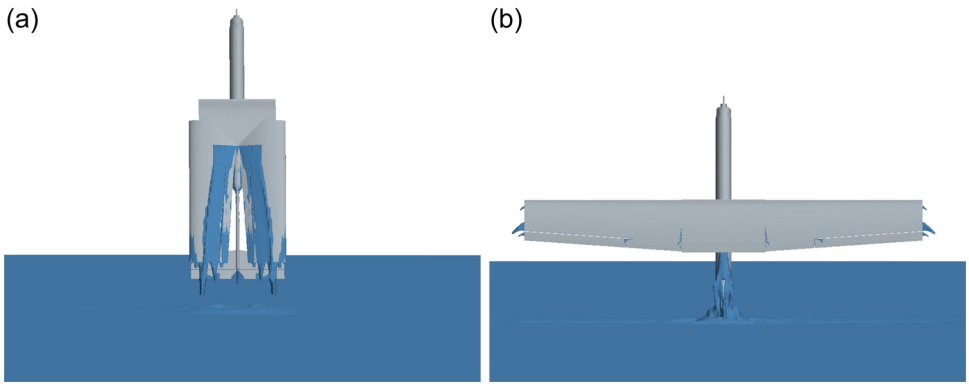

FIGURE 21 Moments of water egress of Longbow II with different wing configurations, where (a) is water egress with folded wings and (b) is water egress with nonfolding wings.

reduce the resistance of underwater navigation, reduce the difficulty of water egress and improve the success rate, the force received by the vehicle when entering the water is reduced, and the influence on the speed of flight is small, but the amount of expandable batteries to be carried becomes smaller. In addition, the presence of foldable wings can reduce the lateral dimension of the LB-II from 2.535 to 0.67 m, see Figure 2, which can significantly reduce the size of the outer package and facilitate the personnel to increase the carrying capacity when using the LB-II to perform the operational tasks, and then be able to efficiently complete the operational tasks. All in all, the presence of foldable wings and propellers in LB-II can have a positive impact.

3 | FIELD TEST AND RESULT ANALYSIS

In the field test, the LB-II was tested in four operations: water sailing, aerial flight, water egress and water ingress. During the test, the vehicle's performance characteristics were recorded by the Pixhawk flight controller, primarily including attitude, depth or altitude, voltage, current, throttle, and other information. Images were captured by ground cameras, a multirotor drone, cell phones, and a first-person camera on the LB-II.

The field tests were conducted in a lake located in Hubei Province, China. Additionally, some of the underwater tests were carried out in the comprehensive test deep pool at Harbin Engineering University.

3.1 | Water sailing operations

As shown in Figure 26, the LB-II maintains a pitch angle of 0° when floating on the water surface, while its positive buoyancy of 0.8 kgf keeps it afloat and ensures the receiver and GPS antenna mounted on the tail remain above the waterline. This allows the vehicle to maintain a continuous GPS signal and provide real-time navigation status to the ground console. Despite the higher wave resistance and slower speed of surface navigation, the testers preferred to use this method to return the LB-II to shore during the field test.

The wings of the LB-II are always folded to reduce drag during underwater navigation. Only the underwater thruster is used for propulsion at this time, while the elevators maintains stable depth and pitch attitude, and the rudder maintains heading stability. The left and right control surfaces of the elevator are deflected at different angles to ensure the stability of LB-II's roll attitude.

The results of the maximum underwater speed test of the LB-II with different air propellers are shown in Table 3. When equipped with a foldable propeller, the propeller blades can be passively folded to a position parallel to the axis of the fuselage, greatly reducing drag during water sailing. When an nonfolding air propeller is installed, the propeller will passively rotate with the vehicle's motion, similar to a windmill, as shown in Figure 27, which is unavoidable and creates more resistance.

The test results reveal that under the same conditions, the wave resistance generated by the water surface significantly reduces the speed of the LB-II. For the LB-II equipped with an nonfolding propeller, even though there is emerging wave resistance during surface navigation, its maximum speed underwater is still slightly lower than the surface speed. This is because when sailing on the surface, only half of the propeller is in the water, which creates water resistance. However, in underwater navigation, the entire propeller faces the current and generates resistance, reducing the speed slightly compared to surface navigation.

Based on the data recorded during several tests, the LB-II's endurance when fully submerged is shown in Table 4. The data was obtained at 100% throttle of the underwater thruster, and endurance was estimated based on the total battery capacity and average power. In practical applications, if the thruster is operated continuously at cruising power, the endurance time will be significantly longer than the time estimated in the table.

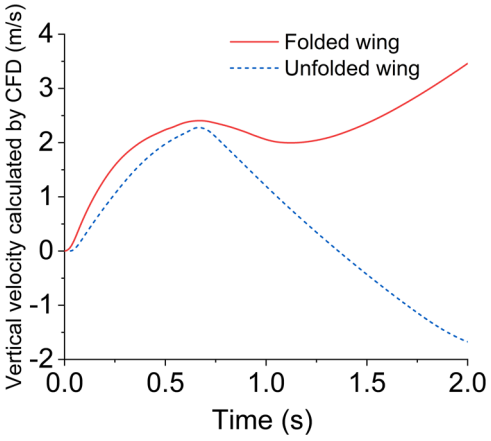

FIGURE 22 Longbow II water exit vertical velocity curves for different wing configurations simulated by computational fluid dynamic.

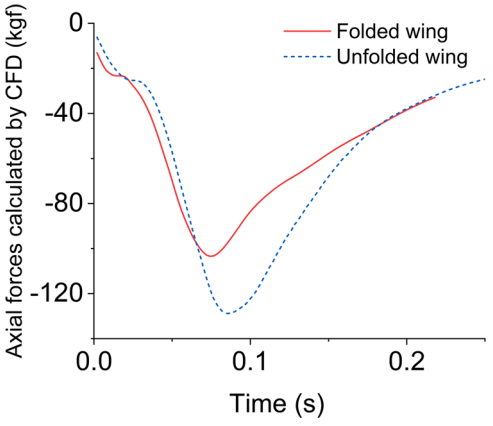

FIGURE 24 Axial force curves of Longbow II at different wing states when entering water.

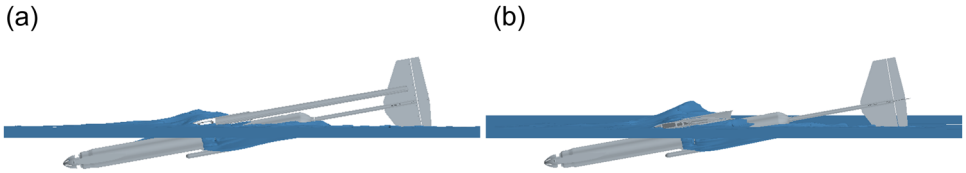

FIGURE 23 Images of Longbow II at the moment of water ingress under computational fluid dynamic simulation, where (a) is the moment of water ingress of the folded wings and (b) is the moment of water ingress of the nonfolding wings.

3.2 | Aerial flight operations

Figure 28 shows a photo of the LB-II equipped with rear three-point landing gear during a flight test, while Figure 29 displays the GPS trajectory of the aerial flight test. Before testing, the load was removed, and additional counterweights and landing gear were installed to maintain the gross weight of 13.3 kg. The test was remotely controlled by the pilot to assess the LB-II's control balance, maneuverability, and structural stability. Flight control parameters were tested and adjusted to ensure automatic control stability after confirming the LB-II met stable flight conditions. When the LB-II is remotely controlled by the pilot, it can be switched at any time between several basic flight modes, such as Manual Mode, Auto Mode, Return Mode, and so on, to facilitate testing.

Based on several flight test data, the range and duration of LB-II air navigation are estimated and presented in Table 5. The results of these tests indicate that the maximum air speed of LB-II is about 44.7 m/s, the minimum speed that can maintain stable flight in the air is about 20 m/s, and the battery energy can be completely depleted to maintain flight for about 10–15 min. Additionally, the LB-II has a maximum range of approximately 20.9 km.

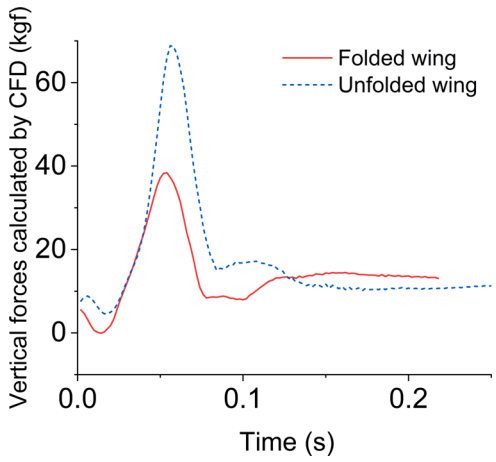

FIGURE 25 Vertical force curves of Longbow II at different wing states when entering water.

3.3 | Water egress operations

3.3.1 | Strategy for water egress

The LB-II always carried a 995 g self-capacitating CTD sensor as a load in the water egress test, with a total weight of 13.3 kg, and a total weight of 13.4 kg with an additional first-person motion camera weighing 104 g.

The transition of the LB-II from underwater to air can be described in Figure 30. First of all, the LB-II sails to a certain depth

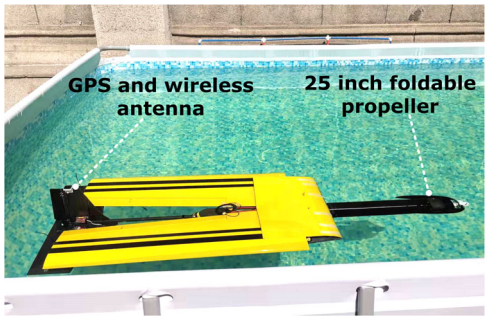

FIGURE 26 Longbow II floating on the water with the foldable propeller installed.

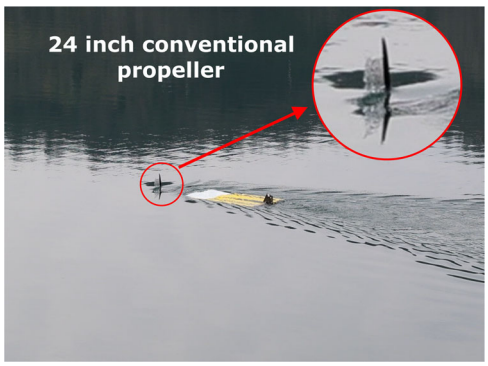

FIGURE 27 Longbow II with nonfolding propeller installed while sailing on the surface.

TABLE 3 Maximum speed of LB-II sailing in water with different propellers.

Status	Air propeller	Maximum speed (m/s)
Surface	Foldable	1.05
Underwater	Foldable	1.23
Surface	Nonfolding	0.99
Underwater	Nonfolding	0.95

TABLE 4 Estimated endurance of LB-II sailing in water at 100% throttle.

Test number	Air propeller	Sailing time (s)	Maximum power (W)	Average power (W)	Estimated endurance (min)
1	Nonfolding	119.9	331.4	295.0	57.8
2	Nonfolding	109.9	313.4	283.5	60.1
3	Foldable	105.0	278.3	250.0	68.2
4	Foldable	114.9	275.3	246.9	69.0

FIGURE 28 Longbow II with landing gear installed.

underwater, and when it reaches the preset depth, it uses the elevator to adjust the airframe to a large pitch angle and floats up until the air propeller is exposed to the surface. Then the air thruster were activated at maximum power and pulled the LB-II out of the water. When the attitude is stabilized the wings will deploy, if the water egress attitude is poor and can never be brought to a stable attitude, the LB-II will stop powering the air thruster and return a water egress failure signal. When the LB-II's wings are smoothly deployed, it will maintain high throttle and enter the climb state, during which it will continuously determine its current state based on information about attitude, altitude, and whether the vehicle is in the water. Once the LB-II judges that the attitude of the airframe is uncontrollable or reenters the water, it will shut down the thruster outputs to protect the vehicle at the hardware level. When the vehicle has successfully climbed to the preset altitude, the vehicle will switch to aerial flight mode and follows a preset path to complete the flight.

As shown in Figure 31, in order for LB-II to rely on the thrust generated by a single air propeller to complete the water egress, the pitch angle of the fuselage should be set as close to 90° as possible so that the propeller thrust in the vertical direction is increased, and the LB-II can leave the water with a lower thrust-to-weight ratio. To have enough depth space to adjust the pitch angle to near vertical, LB-II must sail underwater to a depth of about 6.5 m, and then adjust the pitch angle to near vertical through the elevator and approach the water surface.

During constant depth underwater navigation, the LB-II utilizes the line of sight (LOS) algorithm to calculate the target pitch angle based on the depth error. The calculated angle is then transmitted to the pitch attitude controller, which adjusts the pitch angle of the vehicle to maintain the desired depth. During the depth-holding and water egress phases, the attitude controller employs an integral S-plane algorithm. The integral S-plane algorithm combines the advantages of proportion integration differentiation (PID), offering not only simplicity and ease of parameter tuning but also effective compensation for environmental disturbances on the vehicle's attitude. In particular, during the water egress phase, the vehicle experiences significant disturbances, and the integral S-plane method can achieve good control effectiveness.

Pool tests were conducted to determine the ideal out-of-water pitch angle for the LB-II. A bracket was attached to the bottom of the pool to maintain a constant initial pitch angle for the LB-II underwater. In the initial state, the air propeller was exposed to the water surface and started at full throttle to pull the LB-II out of the water from an initial speed of 0 m/s, as shown in Figure 32.

Subsequently, the test was repeated at different pitch angles by adjusting the bracket. The displacement of the LB-II's nose movement was recorded under different initial water exit angles during the pool test, as shown in Figure 33. The test results show that the ideal water egress angle of the LB-II is approximately between 70° and 85°. Below 70°, the vertical component of the LB-II's propulsion is too small to successfully exit the water. While above 85°, the LB-II is at risk of tipping backward, making it difficult to adjust its attitude.

3.3.2 | Analysis of water egress test phenomena

After LB-II left the water with the wings folded, the fuselage rolled significantly around the longitudinal axis due to the rotational torque of the air thruster and the low air resistance, see Figure 40 from $t = 0.9$ s to $t = 1.8$ s. At this point the wings were not deployed and the ailerons could not play a role in controlling the roll, only the left and right elevator surfaces on the tail could reverse the deflection to resist the counter-torque of the air thruster. It was found in the field test that the elevator surfaces have a better effect in controlling the roll of the LB-II during underwater navigation. However, due to the proximity of the two rudder surfaces to the axis of rotation and the low rudder efficiency caused by the low speed of the LB-II when it just came out of the water. The reverse deflection of the left and right elevator surfaces during the water exit can only slow down the roll caused by the reverse torque, but cannot completely suppress it.

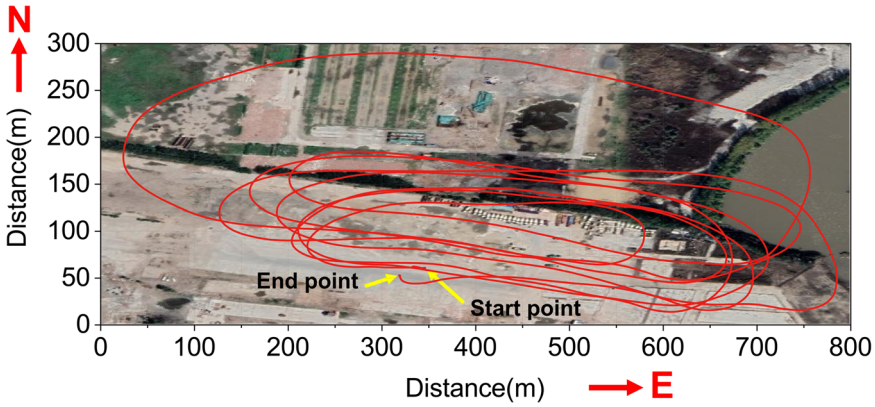

FIGURE 29 GPS track map of land test flight.

TABLE 5 Estimated range and duration of LB-II air flight.

Test number	Flight time (s)	Average throttle (%)	Average speed (m/s)	Average power (W)	Estimated range (km)	Estimated endurance (min)
1	322.5	55.5	23.3	1347.9	17.7	12.6
2	443.6	46.8	23.9	1170.8	20.9	14.6
3	270.8	46.9	23.2	1178.2	20.1	14.5
4	350.2	60.0	28.2	1653.4	17.4	10.3

The spin phenomenon of LB-II at the moment of water departure can be clearly understood from the yaw curve shown in Figure 34, where the yaw angle represents the relative amount of change. When LB-II is at a pitch angle of about 80°, the throttle of the air thruster is opened to 100%, and the counter-torque of the thruster began to act at this time, resulting in a slight change in the yaw angle. When the LB-II fuselage was completely out of the water, drag nearly disappeared and the rate of change of the yaw angle increased significantly. After the air thruster were turned on for 2 s, the wings began to deploy. As the wings gradually deployed, the spinning drag increased significantly, the ailerons were involved in attitude control. As a result, the rate of change of the yaw angle decreased significantly. Once the wings were fully deployed, the yaw angle stabilized, and the LB-II transitioned into the air flight phase.

By comparing the results of several water tests, it is judged that the reasonable time for LB-II to deploy its wings should be 2–2.3 s after the air thruster are activated. During this time, LB-II completes only about one circle of spin, and the pitch angle of LB-II is less than 90° in the positive flight state, and the roll angle is not large, so that the attitude can be more easily adjusted to stability after the wings are deployed.

The other time periods often result in inverted flight and other difficult-to-adjust attitudes, as shown in Figure 35. Due to the low altitude and low speed at the early stage of water egress, making large attitude adjustments can easily lead to stall or insufficient altitude, causing LB-II to fall back into the water, resulting in failed egress.

Figure 36 shows the pitch angle variation curves of several water egress processes in the field test of LB-II. The target pitch angle for these water egress tests was 80°. The air thruster was turned on at 0 s, and the wings began to deploy at 2 s. After the LB-II reached the preset pitch angle of 80°underwater, the elevator continuously adjusted to maintain the pitch angle of the fuselage until the air thruster was engaged. The pitch angle adjustment did not fully converge to the target angle before the thruster was engaged, so the pitch curve fluctuated around 80°. In several tests, the LB-II was successfully released from the water, proving the stability of the water egress at 80° pitch angle.

Figure 37 depicts the depth and pitch angle curves with time for the underwater motion of LB-II before it exited the water. The LB-II system was initiated at 0 s. At 3.8 s, the underwater thruster was activated with 61% throttle and the vehicle began to move forward on the water surface. At 23.7 s, the pitch of the fuselage was adjusted to −35°, and the vehicle dove to a depth of about 6.5 m at 47.0 s. Then, it maintained a depth of 6.5 m for navigation. At 68.7 s, the throttle of the underwater thruster was increased to 94% and the elevator began to deflect to adjust the pitch angle of the fuselage until it reached around 80°. After that, the fuselage maintained a large pitch until the air thruster left the water surface. When the water detection sensor detected the head of LB-II leaving the water surface and the barometer depth value was less than 0.95 m, the air thruster was activated at full speed after the head was 0.2 m out of the water to bring the vehicle out of the water. On the one hand the air thruster is used to get enough traction out of the water as soon as

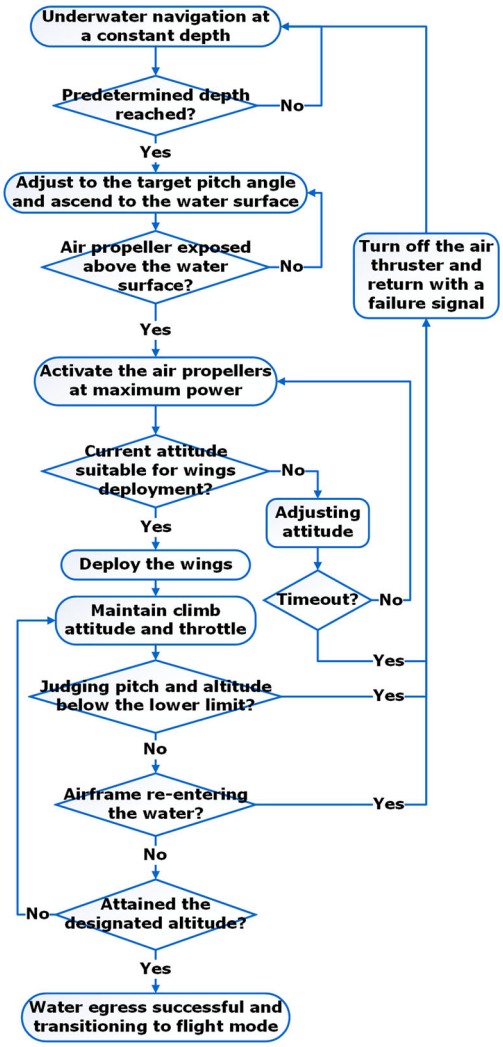

FIGURE 30 Flowchart of Longbow II water egress strategy.

possible, on the other hand the thruster is started above 0.2 m out of the water to avoid damage from the propeller hitting the water surface at high speed. When the tail water sensor detects the tail leaving the water surface, the underwater thruster will be turned off, and the folding mechanism will fully deploy the wings after LB-II reaches a certain height and most of the water has been drained from the wings.

The throttle changes for both the underwater and air thrusters during the test are shown in Figure 38, where the blue dashed line indicates the underwater thruster throttle ratio and the red solid line indicates the air thruster throttle ratio. Before 77.6 s, the vehicle was in the underwater navigation phase, using only the underwater thruster for propulsion. At 77.6 s, the front of the vehicle emerged from the water and the air thruster was activated. At 79.6 s, the stern of the vehicle completely left the water surface, the underwater thruster was deactivated, and the vehicle was propelled solely by the air thruster. After the water egress, LB-II entered the aerial flight phase. During the period of 127.9 s to 137.5 s, the air thruster throttle was completely closed as LB-II was in the stage of high-altitude descent and deceleration. Figure 39 shows photos taken by the first-person camera mounted on LB-II during the test period. Figure 40 and Figure 41 are photographs of the water egress process, with 0 s in Figure 40 representing the moment the air thruster was activated.

The effect of the throttle change on the battery voltage and output current can be seen from the voltage change curve in Figure 42 and the current change curve in Figure 43. During the underwater sailing phase, increasing the throttle of the underwater thruster resulted in a decrease in battery voltage. When the throttle of the air thruster was suddenly increased from 0% to 100%, the voltage dropped drastically to about 39.5 V, and at this time it also generated an instantaneous current peak of 181.8 A. After the peak, the current corresponding to 100% throttle was about 137 A.

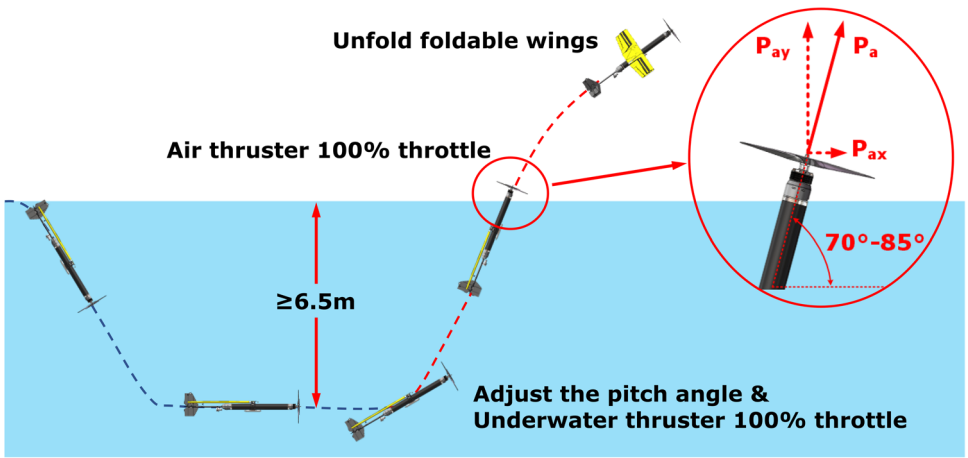

FIGURE 31 Schematic diagram of Longbow II water egress process, where P_a represents the thruster's propulsion, P_{ay} represents the propulsion along the vertical direction component, P_{ax} represents the propulsion along the horizontal direction component, the red dashed line segment in the figure indicates the water egress process.

FIGURE 32 The pool water egress test in the pool with 0 m/s initial velocity and fixed initial pitch angle. (a) Initial angle of 70°, (b) initial angle of 75°, and (c) initial angle of 80°.

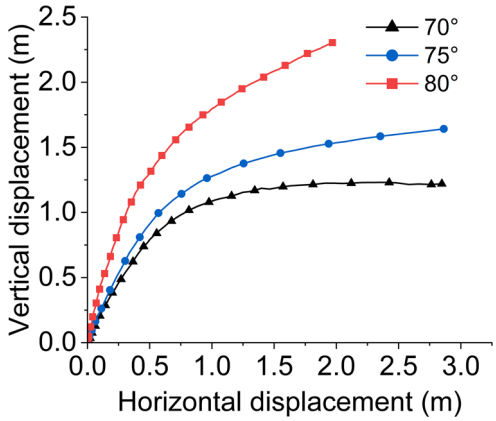

FIGURE 33 Displacement diagram of Longbow II nose with different initial pitch angle of water egress.

FIGURE 35 Longbow II flying upside down due to improper timing of wings deployment.

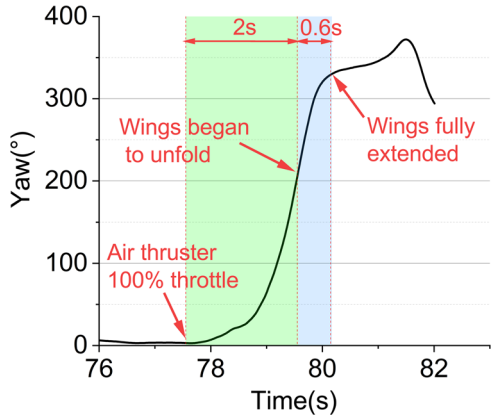

FIGURE 34 Yaw curve at the moment of water exit.

To obtain a higher initial velocity out of the water, the LB-II will increase the throttle of the underwater thruster when adjusting the large pitch angle underwater, as shown in Figure 38. As depicted in Figure 44, the vertical velocity curve indicates that LB-II had an initial velocity of about 1.1 m/s when the air thruster was activated during water egress, and achieved a maximum vertical velocity of around 8.8 m/s as it climbs out of the water. Figure 45 shows the GPS-measured ground speed after leaving the water varied in the range of 19.0–32.5 m/s (excluding the climbing phase out of the water before 85 s in the figure), and the velocity before water ingress is approximately 23.4 m/s, which rapidly dropped to about 0 m/s after approximately 2.8 s. Additionally, Figure 46 demonstrates that the current flight achieved a maximum altitude of around 143.3 m.

3.3.3 | Calculation of energy consumption during the water egress

Table 6 presents data from the seven field tests and summarizes the time, maximum power, and energy consumption for each water egress process. The energy consumption calculation includes the time from when the LB-II begins adjusting the large pitch angle to when the wings are deployed and in a stable flight attitude. Across all seven tests, the water egress process took approximately 13.1–14.6 s, and the average energy consumption for a single water departure was

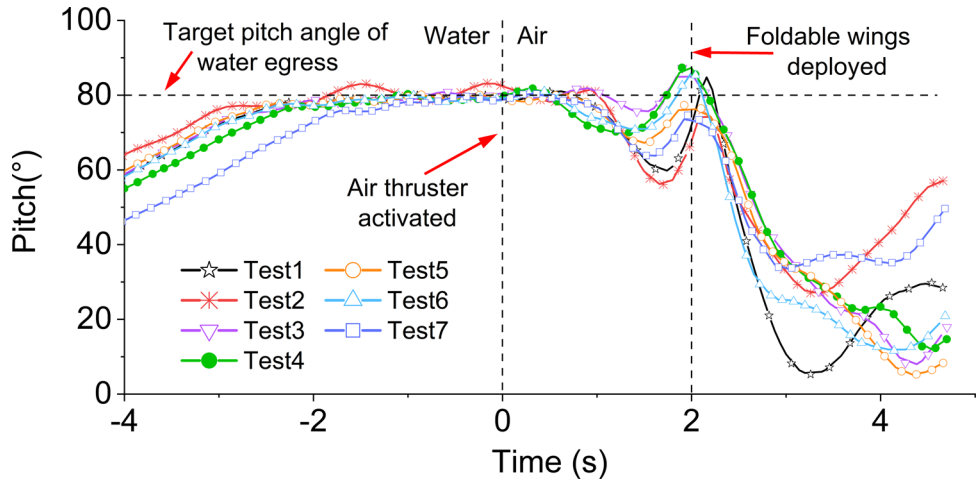

FIGURE 36 Pitch angle variation curves of seven water egress processes in the Longbow II field test.

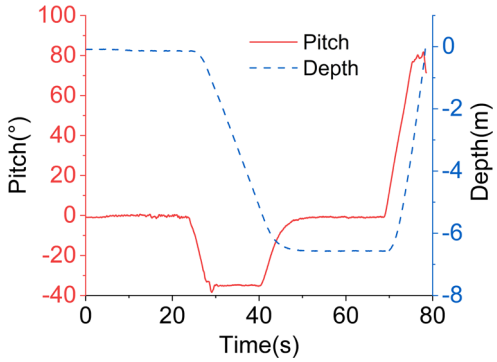

FIGURE 37 Pitch angle and depth change curves of underwater movement before water egress of Longbow II.

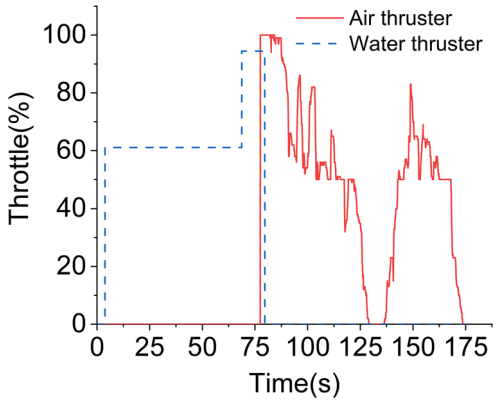

FIGURE 38 Underwater thruster and air thruster throttle variation curves during a complete test of Longbow II.

7.8 Wh. This demonstrates LB-II's rapid trans-medium maneuverability and its ability to operate in multiple mediums within a single flight from an energy perspective.

Notably, the LB-II always carries one CTD during the field tests, which can be removed when other needs arise or more batteries are added to the pressure chamber to extend range. And the LB-II still has the ability to carry other sensors such as a motion camera for operations in an incremental configuration.

3.4 | Water ingress operations

During the field test, two methods were used to complete water ingress: one involved slowing down, gliding, and landing on the water without folding the wings, while the other involved maintaining a smooth attitude at low altitude, slowing down, and then folding the wings into the water. The latter method does not have any automatic or manual control after folding the wings until it enters the water, and the wings must be folded more than 6 m above the water surface to ensure that they can be fully folded before entering the water.

Combining the results of several tests, it was found that the fuselage hardly suffered any damage when entering the water without folding the wings due to the low descent speed and the smooth descent attitude, as shown in Figure 47, where 0 s represents the moment when the LB-II touches the water surface. During several tests, the speed of water ingress was between 18.1 and 26.2 m/s, and the speed reduced to 0 m/s approximately 0.6–1.6 s after contact with the water surface.

In addition to the water ingress speed, the duration of deceleration after entering the water also depends on the pitch

FIGURE 39 First-person view photo of the LB-II field test, (a) shows the moment LB-II emerged from the water, (b) shows the aerial flight phase, and (c) shows the moment of re-entry into the water. LB-II, Longbow II.

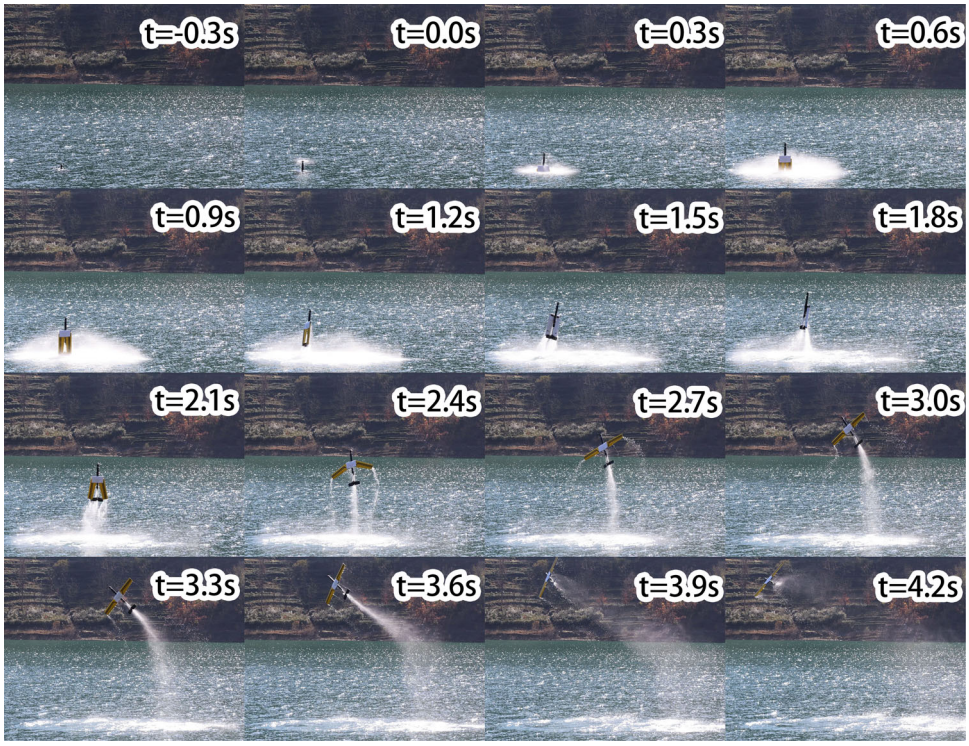

FIGURE 40 Changes of motion state of Longbow II water egress process.

FIGURE 41 Synthesis diagram of Longbow II attitude changes during the water egress process.

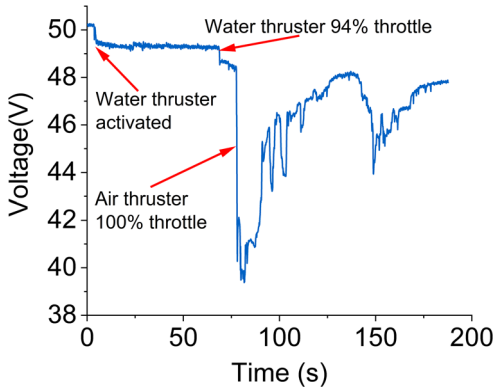

FIGURE 42 Voltage change curve during a complete test of Longbow II.

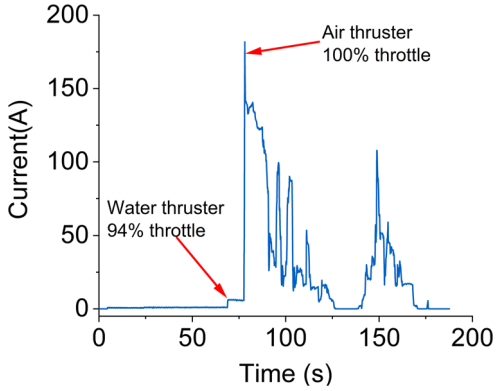

FIGURE 43 Current change curve during a complete test of Longbow II.

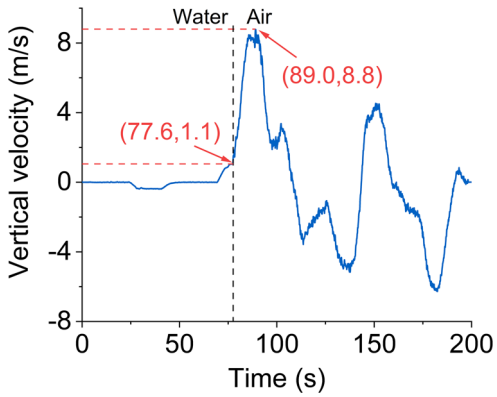

FIGURE 44 Vertical velocity variation curve during a complete test of Longbow II.

angle during water ingress. When the pitch angle is around 0 degrees or greater than 0°, the LB-II is more likely to bounce upwards after contacting the water surface, resulting in a slightly longer

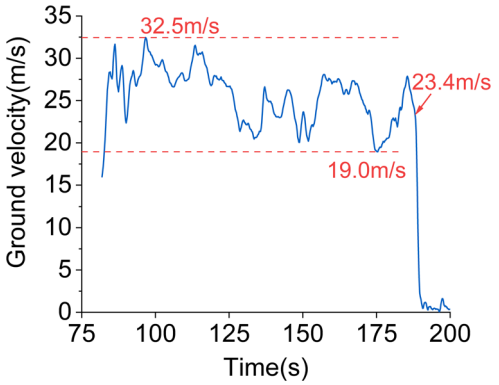

FIGURE 45 Ground speed variation curve during a complete test of Longbow II.

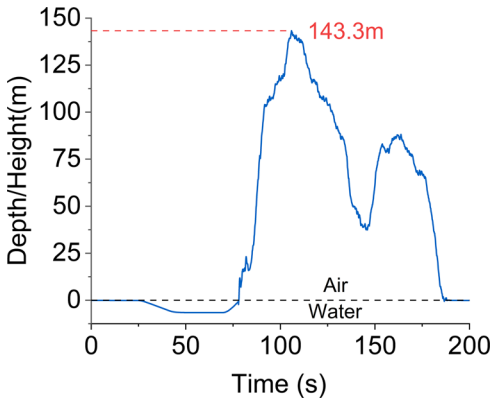

FIGURE 46 Depth and height variation curve during a complete test of Longbow II.

deceleration time, as shown in Figure 48. On the other hand, when the pitch angle is significantly less than 0°, the nose of the LB-II is pointed downward, and it is easier to penetrate the water surface, resulting in a faster deceleration after entering the water.

The roll angle, pitch angle, and vertical acceleration profiles corresponding to the water ingress test in Figure 47 are shown in Figure 49. Since the accuracy of the accelerometer is limited, the accelerometer curve here is primarily used to demonstrate the changing trend of the impact experienced by the vehicle upon entering the water. Due to the presence of gravity, the accelerometer will always record an acceleration of −9.8 m/s² when LB-II is stationary. From the acceleration variation curve, two obvious acceleration fluctuations can be observed, indicating that LB-II suffered a secondary impact from the water surface during the water entry process. The first contact with the water surface consumed most of LB-II's kinetic energy, making the second impact significantly smaller than the first. From the attitude angle curve, it can be seen that the vehicle rolled and pitched smoothly during the

TABLE 6 Estimated energy consumption for the water egress tests.

Test number	Air propeller	Water egress time (s)	Maximum power (W)	Energy consumption (Wh)
1	Foldable	13.6	6675.3	8.9
2	Nonfolding	13.1	7436.6	6.9
3	Nonfolding	14.6	7305.8	8.7
4	Nonfolding	14.5	7267.0	9.2
5	Nonfolding	13.6	6485.7	6.7
6	Nonfolding	13.3	6723.1	6.6
7	Nonfolding	14.0	6439.2	7.8

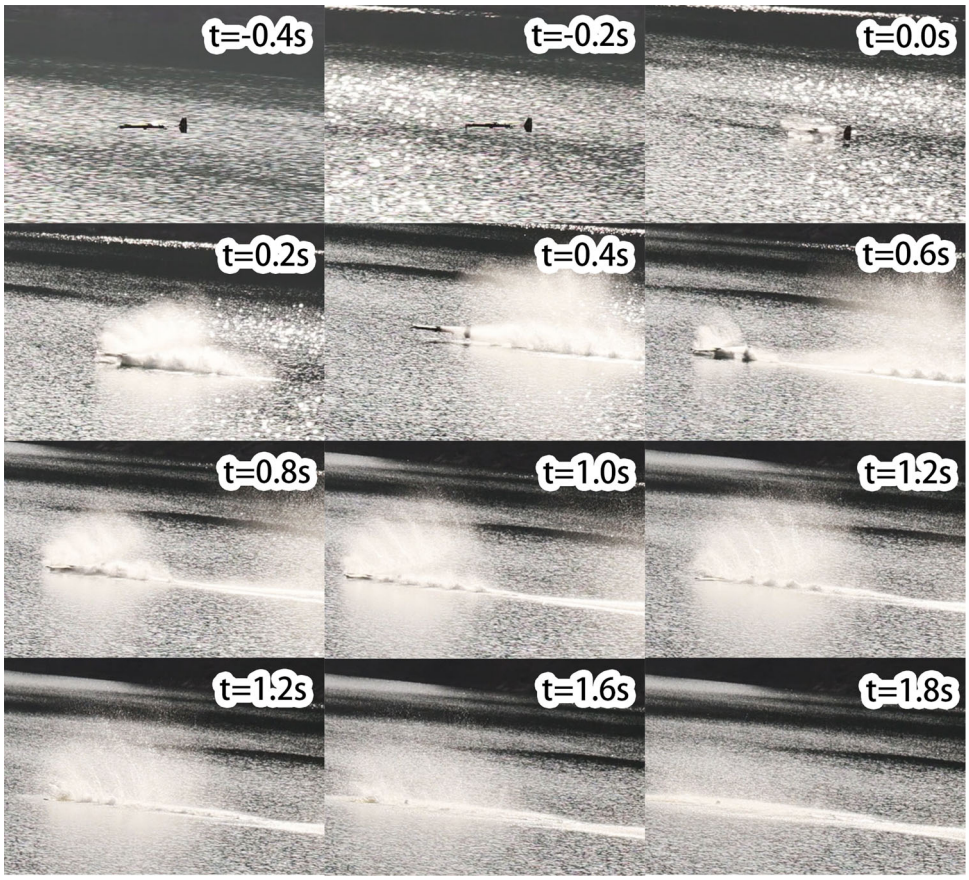

FIGURE 47 Changes in motion state during water entry with Longbow II wings unfolded.

water entry process without folding the wings, with fluctuations of less than 5°.

After entering the water, the LB-II can fold its wings in the water to continue other operational tasks. The disadvantage of not folding the wings into the water is the need to properly reduce the LB-II flight speed and maintain a smoother descent attitude before entering the water, and to make the forces on the left and right sides of the fuselage as close as possible when entering the water to avoid structural damage. With the current flight control algorithms, it is relatively easy to achieve a smoother glide and enter the water without folding the wings. Therefore, in the initial tests, the LB-II will more often enter the

FIGURE 48 Longbow II bouncing up after entering the water and slamming the water surface.

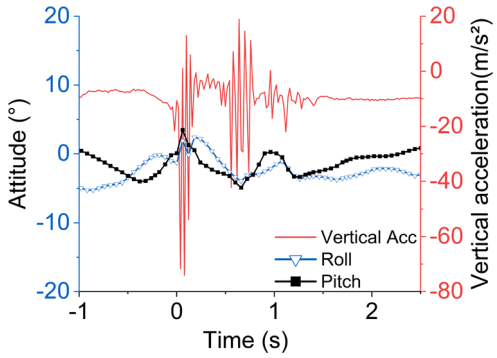

FIGURE 49 Attitude and acceleration curves at moment of water entry with Longbow II wings unfolded.

water without folding its wings to reduce the risk of structural damage.

The water ingress of the folded wings was also tested during the field test, as shown in Figure 50. The photo was taken by a multirotor drone from a top-down perspective, capturing the shadow of LB-II on the water surface. The moment when LB-II touches the water surface is represented as 0 s. The wings were folded when LB-II was approximately 6 m above the water surface, after which LB-II was allowed to enter the water freely without applying any control, reaching an instantaneous speed of about 26.9 m/s, and completing deceleration after about 0.8 s. The attitude angle and acceleration curves are shown in Figure 51. The instantaneous vertical acceleration at water entry was significantly higher than that of the unfolded wings. This is due to the slightly higher horizontal speed at the moment of entry with the folded wings, and the stronger impact at 6 m above the water surface due to the complete lack of control of the vertical speed.

After the wings were folded, the LB-II made an almost level throw, and the pitch angle decreased slightly before it touched the water surface. Although the motor had stopped running by this time, the nonfolding propeller continued to rotate passively against the wind, similar to a windmill, and the resulting spin torque caused a significant change in the roll angle of the fuselage. As a result, the nose of the LB-II entered the water first, followed by the left side of the fuselage before the right side. Once in the water, the LB-II quickly regained a stable attitude.

During the subsequent structural inspection, it was found that the fairing shell section between the two wings of the LB-II had sustained slight damage, with the screw holes torn and deformed by strong external forces. No other parts of the fuselage were found to be defective. The reason why this phenomenon did not occur when the wings were unfolded in the water is because, in that configuration, both sides of the wings and the fairing shell are subjected to the impact of the water together. Moreover, the strength of the wings is much higher than that of the fairing shell. Additionally, the two ends of the fairing shells rest on the wings on both sides, making the support more solid.

Folding the wings and then entering the water makes the wings well protected, but the fairing section bears the brunt of the damage and is more prone to damage. The advantage of folding the wings when entering the water is that it is not necessary to maintain a smooth attitude to lower the altitude, and the wings can be folded at a certain height above the water surface to enter the water quickly and without the need to control. Therefore, when pursuing high-speed water entry under folded wings conditions, the fairing support structure should be strengthened first to mitigate the damage it may sustain.

4 | CONCLUSION

This paper presents the design and field test of a new foldable wing UAUV. Based on the fixed-wing UAUV, the rapidly foldable wings are designed and combined with a large pitch angle water egress and attitude adjustment strategy, which successfully solves the problems of high resistance to underwater navigation and high difficulty of fixed-wing UAUV water egress, reduces the extreme requirements of thrust of propulsion in the past, and has the ability of low thrust-to-weight ratio for water egress.

Through field tests, the LB-II has demonstrated its ability to carry out both underwater and air operations under load conditions, and to perform trans-medium transitions during water egress and ingress, achieving the design objectives. This paper presents a detailed analysis of a series of test data collected during the field tests, allowing for an understanding of the

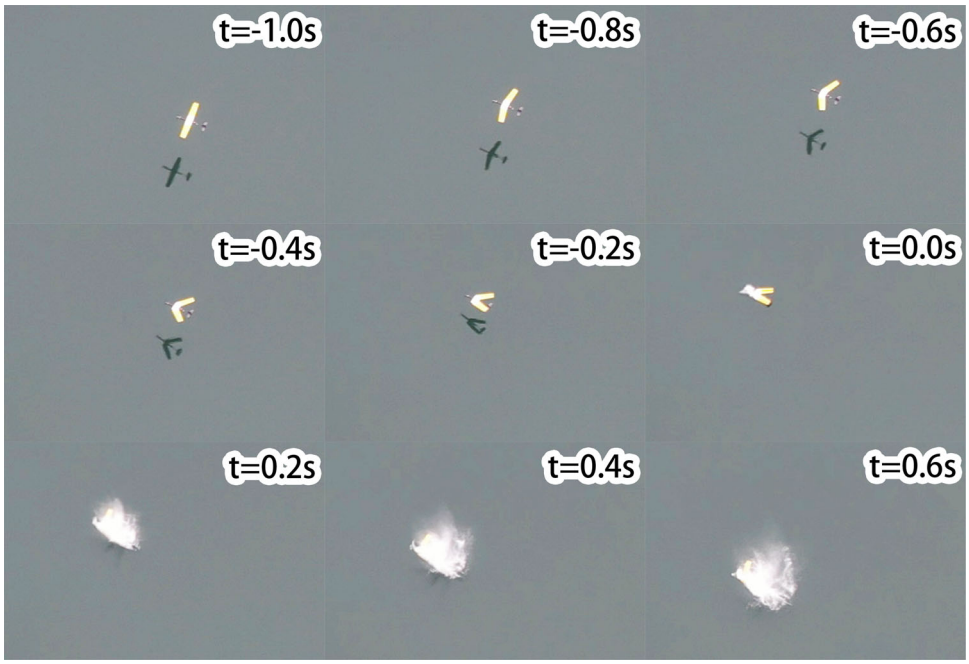

FIGURE 50 Changes in motion state during water entry with Longbow II wings folded.

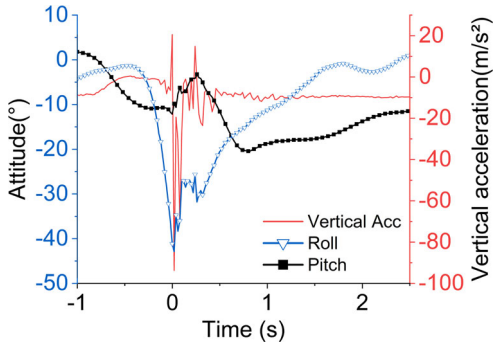

FIGURE 51 Attitude and acceleration curves at moment of water entry with Longbow II wings folded.

performance characteristics of the LB-II during underwater, air, water egress and ingress processes, as well as identifying its strengths and weaknesses. Furthermore, calculations have been made on the flight range and endurance time under various motion states, providing important experience and data references for the development of fixed-wing UAUVs in the future.

The designed wing folding mechanism enables the wings to complete the folding and unfolding action in 0.6 s. The mechanism resists the huge impact brought by the wings when they enter the water and can maintain the self-locking of the structure and stability of the mechanism. This proves the rationality of the design and becomes an important guarantee for the successful trans-medium water egress and ingress. In actual tests, LB-II was able to successfully exit the water with a minimum thrust-to-weight ratio of about 1.30, demonstrating the necessity of the folding wings and the effectiveness of the large pitch angle water exit method.

The LB-II was always loaded with a self-capacitance CTD sensor during the field test, and it was able to successfully complete the trans-medium navigation tasks. In future tests, this payload can be flexibly replaced. The remaining space in the pressure-resistant cabin can be used to carry batteries of appropriate weight for testing longer range endurance. Alternatively, multiple other sensors can be mounted to test the engineering application of fixed-wing UAUVs.

During the water egress test, a spinning phenomenon was observed before the wings unfolding, which caused a series of problems, such as the timing of wings unfolding during spinning and pitch angle fluctuations after spinning. Although these issues have been appropriately addressed in the experiment, future improvements can be made to solve this problem. For instance, increase the area of the left and right rudder surfaces to improve the rudder efficiency of the water exit process to resist spin. Additionally, more accurate and reliable sensors for measuring attitude, acceleration, depth, altitude and speed can be used at the sensor level, allowing the processor to obtain current status information promptly and accurately. At the software level, the water exit control algorithm can be further optimized to enable more accurate and timely adjustments for the target attitude.

During the experiments, the foldable propeller form has proven to be suitable for use on the LB-II, as the resistance during underwater navigation was significantly reduced and the underwater speed was significantly increased after folding. The foldable propeller is helpful for both high-speed underwater propulsion and long-distance energy-saving navigation. However, the currently used foldable propeller has low efficiency, lower thrust under the same power. Therefore, a high-efficiency foldable propeller should be designed specifically for the LB-II in the future. In addition, the strength of the installation structure of the fairing should be appropriately increased to cope with the high-intensity impact of the folding wings entering the water.

During field tests, LB-II is primarily deployed on the water surface or hand-launched, and recovered by water landing. Catapult launch, as well as net recovery, could be tested in future tests, allowing rapid deployment and recovery on small space platforms such as ships.

ACKNOWLEDGMENTS

The authors gratefully acknowledge the help provided by Zhaoliang Han, Haibo Li and Feng Jin in the field tests. The authors also acknowledge the support for the study from the foundation of the Hainan Provincial Joint Project of Sanya Yazhou Bay Science and Technology City (No: 520LH007), the National Natural Science Foundation of China (No. 52071104), and the Stable Supporting Fund of Science and Technology on Underwater Vehicle Technology (JCKYS2023SXJQR-02).

DATA AVAILABILITY STATEMENT

The data that support the findings of this study are available on request from the corresponding author. The data are not publicly available due to privacy or ethical restrictions.

ORCID

Xiangren Sun http://orcid.org/0009-0005-8398-3931
Ye Li http://orcid.org/0000-0002-5609-7388

REFERENCES

Alzu'bi, H., Mansour, I. & Rawashdeh, O. (2018) Loon copter: implementation of a hybrid unmanned aquatic–aerial quadcopter with active buoyancy control. *Journal of Field Robotics*, 35(5), 764–778. Available from: https://doi.org/10.1002/rob.21777

Canelon-Suarez, D., Wang, Y. & Papanikolopoulos, N. (2020) Omnibot: a small versatile robotic platform capable of air, ground, and underwater operation. In: *2020 International Conference on Unmanned Aircraft Systems (ICUAS)*. Athens, Greece: IEEE. pp. 1742–1747. https://doi.org/10.1109/ICUAS48674.2020.9214021

Carlton, J.S. (2019) *Marine propellers and propulsion*, 4th edition. Butterworth-Heinemann.

Farinha, A., Di Tria, J., Zufferey, R., Armanini, S.F. & Kovac, M. (2021). Challenges in control and autonomy of unmanned aerial-aquatic vehicles. In: *2021 29th Mediterranean Conference on Control and Automation (MED)*. Puglia, Italy: IEEE. pp. 937–942. https://doi.org/10.1109/MED51440.2021.9480342

Kim, H.J., Kim, M., Lim, H., Park, C., Yoon, S., Lee, D. et al. (2013) Fully autonomous vision-based net-recovery landing system for a fixed-wing UAV. *IEEE/ASME Transactions on Mechatronics*, 18(4), 1320–1333. Available from: https://doi.org/10.1109/TMECH.2013.2247411

Li, L., Wang, S., Zhang, Y., Song, S., Wang, C., Tan, S. et al. (2022) Aerial-aquatic robots capable of crossing the air-water boundary and hitchhiking on surfaces. *Science Robotics*, 7(66), eabm6695. Available from: https://doi.org/10.1126/scirobotics.abm6695

Liang, J., Yang, X., Wang, T., Yao, G. & Zhao, W. (2013) Design and experiment of a bionic gannet for plunge-diving. *Journal of Bionic Engineering*, 10(3), 282–291. Available from: https://doi.org/10.1016/S1672-6529(13)60224-3

Liang, J., Yao, G., Wang, T., Yang, X., Zhao, W., Song, G. et al. (2014) Wing load investigation of the plunge-diving locomotion of a gannet morus inspired submersible aircraft. *Science China: Technological Sciences*, 57(2), 390–402. Available from: https://doi.org/10.1007/s11431-013-5437-5

Lu, D., Xiong, C., Lyu, B., Zeng, Z. & Lian, L. (2018) Multi-mode hybrid aerial underwater vehicle with extended endurance. In: *2018 OCEANS—MTS/IEEE Kobe Techno-Oceans (OTO)*. Kobe, IEEE. pp. 1–7. https://doi.org/10.1109/OCEANSKOBE.2018.8559438

Lu, D., Xiong, C., Zeng, Z. & Lian, L. (2019) A multimodal aerial underwater vehicle with extended endurance and capabilities. In: *2019 International Conference on Robotics and Automation (ICRA)*. Montreal, QC, Canada: IEEE. pp. 4674–4680. https://doi.org/10.1109/ICRA.2019.8793985

Lu, D., Xiong, C., Zhou, H., Lyu, C., Hu, R., Yu, C. et al. (2021) Design, fabrication, and characterization of a multimodal hybrid aerial underwater vehicle. *Ocean Engineering*, 219, 108324. Available from: https://doi.org/10.1016/j.oceaneng.2020.108324

Maia, M.M., Mercado, D.A. & Diez, F.J. (2017) Design and implementation of multirotor aerial-underwater vehicles with experimental results. In: *2017 IEEE/RSJ International Conference on Intelligent Robots and Systems (IROS)*. Vancouver, BC: IEEE. pp. 961–966. https://doi.org/10.1109/IROS.2017.8202261

Molland, A.F., Turnock, S.R. & Hudson, D.A. (2017) *Ship resistance and propulsion: practical estimation of ship propulsive power*, 2nd edition. Cambridge University Press. Available from: https://doi.org/10.1017/9781316494196

Rockenbauer, F., Jeger, S., Beltran, L., Berger, M., Harms, M., Kaufmann, N. et al. (2021) Dipper: a dynamically transitioning aerial-aquatic unmanned vehicle. *Robotics: Science and Systems*, 2021, 12–16. Available from: https://doi.org/10.15607/RSS.2021.XVII.048

Siddall, R. & Kovac, M. (2015) A water jet thruster for an aquatic micro air vehicle. In: *2015 IEEE International Conference on Robotics and Automation (ICRA)*. Seattle, WA, USA: IEEE. pp. 3979–3985. https://doi.org/10.1109/ICRA.2015.7139755

Siddall, R. & Kovac, M. (2017) Fast aquatic escape with a jet thruster. *IEEE/ASME Transactions on Mechatronics*, 22(1), 217–226. Available from: https://doi.org/10.1109/TMECH.2016.2623278

Siddall, R. & Kovač, M. (2014) Launching the AquaMAV: bioinspired design for aerial–aquatic robotic platforms. *Bioinspiration & Biomimetics*, 9(3), 031001. Available from: https://doi.org/10.1088/1748-3182/9/3/031001

Siddall, R., Ortega Ancel, A. & Kovač, M. (2017) Wind and water tunnel testing of a morphing aquatic micro air vehicle. *Interface Focus*, 7(1), 20160085. Available from: https://doi.org/10.1098/rsfs.2016.0085

Skulstad, R., Syversen, C., Merz, M., Sokolova, N., Fossen, T. & Johansen, T. (2015) Autonomous net recovery of fixed-wing UAV with single-frequency carrier-phase differential GNSS. *IEEE Aerospace and Electronic Systems Magazine*, 30(5), 18–27. Available from: https://doi.org/10.1109/MAES.2015.7119821

Stewart, W., Weisler, W., Anderson, M., Bryant, M. & Peters, K. (2020) Dynamic modeling of passively draining structures for aerial–aquatic unmanned vehicles. *IEEE Journal of Oceanic Engineering*, 45(3),

840–850. Available from: https://doi.org/10.1109/JOE.2019.2898069

Stewart, W., Weisler, W., MacLeod, M., Powers, T., Defreitas, A., Gritter, R. et al. (2018) Design and demonstration of a seabird-inspired fixed-wing hybrid UAV-UUV system. *Bioinspiration & Biomimetics*, 13(5), 056013. Available from: https://doi.org/10.1088/1748-3190/aad48b

Tan, Y.H. & Chen, B.M. (2019a) Design of a morphable multirotor aerial-aquatic vehicle. In: *OCEANS 2019 MTS/IEEE SEATTLE*, Seattle, WA, USA: IEEE. pp. 1–8. https://doi.org/10.23919/OCEANS40490.2019.8962867

Tan, Y.H. & Chen, B.M. (2019b) Motor-propeller matching of aerial propulsion systems for direct aerial-aquatic operation. In: *2019 IEEE/RSJ International Conference on Intelligent Robots and Systems (IROS)*, Macau, China: IEEE. 1963–1970. https://doi.org/10.1109/IROS40897.2019.8968257

Tan, Y.H., Siddall, R. & Kovac, M. (2017) Efficient aerial–aquatic locomotion with a single propulsion system. *IEEE Robotics and Automation Letters*, 2(3), 1304–1311. Available from: https://doi.org/10.1109/LRA.2017.2665689

Wei, T., Lu, D., Zeng, Z. & Lian, L. (2022) Trans-media kinematic stability analysis for hybrid unmanned aerial underwater vehicle. *Journal of Marine Science and Engineering*, 10(2), 275. Available from: https://doi.org/10.3390/jmse10020275

Wei, Z., Teng, Y., Meng, X., Yao, B. & Lian, L. (2022) Lifting-principle-based design and implementation of fixed-wing unmanned aerial–underwater vehicle. *Journal of Field Robotics*, 39(6), 694–711. https://doi.org/10.1002/rob.22071

Weisler, W., Stewart, W., Anderson, M.B., Peters, K.J., Gopalarathnam, A. & Bryant, M. (2018) Testing and characterization of a fixed wing cross-domain unmanned vehicle operating in aerial and underwater environments. *IEEE Journal of Oceanic Engineering*, 43(4), 969–982. Available from: https://doi.org/10.1109/JOE.2017.2742798

Yang, X., Wang, T., Liang, J., Yao, G. & Liu, M. (2015) Survey on the novel hybrid aquatic–aerial amphibious aircraft: aquatic unmanned aerial vehicle (AquaUAV. *Progress in Aerospace Sciences*, 74, 131–151. Available from: https://doi.org/10.1016/j.paerosci.2014.12.005

Yang, X., Wang, T., Liang, J., Yao, G. & Zhao, W. (2013) Submersible unmanned aerial vehicle concept design study. In: *2013 Aviation Technology, Integration, and Operations Conference*, Los Angeles, CA. 4422. https://doi.org/10.2514/6.2013-4422

Yao, G., Liang, J., Wang, T., Yang, X., Liu, M. & Zhang, Y. (2014) Submersible unmanned flying boat: design and experiment. In: *2014 IEEE International Conference on Robotics and Biomimetics (ROBIO 2014)*. Bali, Indonesia: IEEE. pp. 1308–1313. https://doi.org/10.1109/ROBIO.2014.7090514

Zeng, Z., Lyu, C., Bi, Y., Jin, Y., Lu, D. & Lian, L. (2022) Review of hybrid aerial underwater vehicle: cross-domain mobility and transitions control. *Ocean Engineering*, 248, 110840. Available from: https://doi.org/10.1016/j.oceaneng.2022.110840

Zha, J., Thacher, E., Kroeger, J., Makiharju, S.A. & Mueller, M.W. (2019) Towards breaching a still water surface with a miniature unmanned aerial underwater vehicle. In: *2019 International Conference on Unmanned Aircraft Systems (ICUAS)*, Atlanta, GA, USA: IEEE. pp. 1178–1185. https://doi.org/10.1109/ICUAS.2019.8798350

Zufferey, R., Ancel, A.O., Farinha, A., Siddall, R., Armanini, S.F., Nasr, M. et al. (2019) Consecutive aquatic jump-gliding with water-reactive fuel. *Science Robotics*, 4(34), eaax7330. Available from: https://doi.org/10.1126/scirobotics.aax7330

SUPPORTING INFORMATION

Additional supporting information can be found online in the Supporting Information section at the end of this article.

How to cite this article: Sun, X., Cao, J., Li, Y. & Wang, B. (2024) Design and field test of a foldable wing unmanned aerial–underwater vehicle. *Journal of Field Robotics*, 41, 347–373. https://doi.org/10.1002/rob.22265